

Investigating the Applicability of Emergent Constraints

Alexander J. Winkler^{1,2}, Ranga B. Myneni³, and Victor Brovkin¹

¹Max Planck Institute for Meteorology, Bundesstrasse 53, 20146 Hamburg, Germany

²International Max Planck Research School on Earth System Modelling, Bundesstrasse 53, 20146 Hamburg, Germany

³Department of Earth and Environment, Boston University, Boston, Massachusetts 02215, USA

Correspondence: Alexander J. Winkler (alexander.winkler@mpimet.mpg.de)

1 **Abstract.**

2 Recent research on Emergent Constraints (EC) has delivered promising results in narrowing down uncertainty in climate pre-
3 dictions. The method utilizes a measurable variable (predictor) from the recent historical past to obtain a constrained estimate
4 of change in an entity of interest (predictand) at a potential future CO₂ concentration (forcing) from multi-model projections.
5 This procedure critically depends on, first, accurate estimation of the predictor from observations and models, and second, on
6 a robust relationship between inter-model variations in the predictor-predictand space. Here, we investigate issues related to
7 these two themes in a carbon cycle case study using observed vegetation greening sensitivity to CO₂ forcing as a predictor
8 of change in photosynthesis (Gross Primary Productivity, GPP) for a doubling of pre-industrial CO₂ concentration. Greening
9 sensitivity is defined as changes in annual maximum of green leaf area index (LAI_{max}) per unit CO₂ forcing realized through
10 its radiative and fertilization effects. We first address the question of how to realistically characterize the predictor of a large
11 area (e.g. greening sensitivity in the northern high latitudes region) from pixel-level data. This requires an investigation into
12 uncertainties in the observational data source and an evaluation of the spatial and temporal variability in the predictor in both
13 the data and model simulations. Second, the predictor-predictand relationship across the model ensemble depends on a strong
14 coupling between the two variables, i.e. simultaneous changes in GPP and LAI_{max}. This coupling depends in a complex man-
15 ner on the magnitude (level), time-rate of application (scenarios) and effects (radiative and/or fertilization) of CO₂ forcing. We
16 investigate how each one of these three aspects of forcing can affect the EC estimate of the predictand (Δ GPP). Our results
17 show that uncertainties in the EC method primarily originate from a lack of predictor comparability between observations
18 and models, the observational data source, and temporal variability of the predictor. The disagreement between models on the
19 mechanistic behavior of the system under intensifying forcing limits the EC applicability. The discussed limitations and sources
20 of uncertainty in the EC method go beyond carbon cycle research and are generally applicable in Earth system sciences.

21 *Copyright statement.*

1 1 Introduction

2 Earth system models (ESMs) are powerful tools to predict responses to a variety of forcings such as increasing atmospheric
3 concentration of greenhouse gases and other agents of radiative forcing (Klein and Hall, 2015). Still, longterm ESM projections
4 of climate change have substantial uncertainties. This can be due to poorly understood processes in some cases, and in others,
5 to missing or simplified representations called parameterizations (Flato et al., 2013; Klein and Hall, 2015; Knutti et al., 2017).
6 Certain important processes, especially in the atmosphere, happen at spatial scales finer than can be possibly represented in
7 current ESMs. Consequently, various phenomena in the system ranging from local extreme precipitation events to large-scale
8 climate modes, can be poorly simulated (Flato et al., 2013). Errors propagate and can be amplified through feedbacks among
9 interacting components in the Earth system, resulting in biases whose origins can be difficult to identify (Flato et al., 2013).
10 Furthermore, an inherent component of the Earth climatic system, its internal natural variability, is complicated to represent
11 and simulate in models (Flato et al., 2013; Klein and Hall, 2015).

12

13 Model Intercomparison Projects explore these uncertainties by coordinating a wide range of simulation setups focusing on
14 internal variability, boundary conditions, parameterizations, etc. (Taylor et al., 2012; Flato et al., 2013; Eyring et al., 2016;
15 Knutti et al., 2017). Models developed at various institutions are driven with the same forcing information (e.g. historical forc-
16 ing) or with identical idealized boundary conditions. However, each modeling group decides which of the processes to consider
17 and implement in their ESM. The conventional approach of handling these multi-model ensembles is to use unweighted ensem-
18 ble averages (Knutti, 2010; Knutti et al., 2017). This assumes that the models are independent of one another and equally good
19 at simulating the climate system (Flato et al., 2013; Knutti et al., 2017). The large spread between model projections suggests
20 that this assumption is not valid. Therefore, alternate methods have been developed to extract results more accurate than multi-
21 model averages (e.g. model weighting scheme based on performance and interdependence, Knutti et al., 2017). The concept of
22 *Emergent Constraints* arises in this context, namely, as a method to reduce uncertainty in ESM projections relying on histori-
23 cal simulations and observations (Hall and Qu, 2006; Boé et al., 2009; Cox et al., 2013; Klein and Hall, 2015; Cox et al., 2018).

24

25 The two key parts of an Emergent Constraint (EC) based method are a linear relationship arising from the collective behavior
26 of a multi-model ensemble and an observational estimate for imposing the said constraint (Fig. 1). The linear relationship is a
27 physically (or physiologically) based correlation between inter-model variations in an observable entity of the contemporary
28 climate system (*predictor*) and a projected variable (*predictand*) that is difficult to observe or not observable at all. Combining
29 the emergent linear relationship with observations of the predictor sets a constraint on the predictand (Cox et al., 2013; Flato
30 et al., 2013; Klein and Hall, 2015; Knutti et al., 2017). Many such ECs have been identified and reported, as briefly summarized
31 below.

32

33 Hall and Qu (2006) proposed a constraint on projections of snow-albedo feedback based on the correlation between large
34 inter-model variations in feedback strength of the current seasonal cycle. The EC was first established for the CMIP3 ensemble

1 and confirmed for phase five of the Coupled Model Intercomparison Project (CMIP5; Flato et al., 2013; Qu and Hall, 2014).
2 Several EC studies followed with the goal of reducing uncertainty in projections of the cloud feedback under global warming,
3 as reviewed by Klein and Hall (2015). It is thought that erroneous representation of low-cloud feedback in ESMs contributes
4 essentially to the large uncertainty in equilibrium climate sensitivity (ECS, 1.5 to 5 K), i.e. warming for a doubling of pre-
5 industrial atmospheric CO₂ concentration (2×CO₂; Sherwood et al., 2014; Klein and Hall, 2015). Recently, Cox et al. (2018)
6 presented a different approach to constrain ECS based on its relationship to variability of global temperatures during the recent
7 historical warming period. They reported a constrained ECS estimate of 2.8 K for 2×CO₂ (66% confidence limits of 2.2 – 3.4
8 K).

9
10 The concept of EC also found its way into the field of carbon cycle projections. A series of studies analyzed the extent
11 to which inter-annual atmospheric CO₂ variability can serve as a predictor of longterm temperature sensitivity of terrestrial
12 tropical carbon storage. Cox et al. (2013) and Wenzel et al. (2014) reported an emergent linear relationship, although with
13 different slopes for CMIP3 and CMIP5 ensembles, resulting in slightly divergent constrained estimates (CMIP3: -53 ± 17 Pg
14 C K⁻¹, CMIP5: -44 ± 14 Pg C K⁻¹). Wang et al. (2014) however were unable to detect a similar relationship between the
15 proposed predictor and predictand. Recently, Lian et al. (2018) presented an EC estimate of the global ratio of transpiration
16 to total terrestrial evapotranspiration (T/ET), which is substantially higher (0.62 ± 0.06) than the unconstrained value ($0.41 \pm$
17 0.11). For the marine tropical carbon cycle, Kwiatkowski et al. (2017) identified an emergent relationship between the longterm
18 sensitivity of tropical ocean net primary production (NPP) to rising sea surface temperature (SST) in the equatorial zone and
19 the interannual sensitivity of NPP to El Niño/Southern Oscillation driven SST anomalies. Tropical NPP is projected to decrease
20 by $3 \pm 1\%$ for 1 K increase in equatorial SST according to the observational constraint.

21
22 Similar results were reported for modeled extra-tropical terrestrial carbon fixation in a 2×CO₂ world. Plant productivity is
23 expected to increase due to the fertilizing and radiative effects of rising atmospheric CO₂ concentration. Wenzel et al. (2016)
24 focused on constraining the CO₂ fertilization effect on plant productivity in the northern high latitudes (60° N – 90° N, NHL)
25 and the entire extra-tropical area in the northern hemisphere (30° N – 90° N) using the seasonal amplitude of longterm CO₂
26 measurements at different latitudes. They presented a linear relationship between the sensitivity of CO₂ amplitude to rising
27 atmospheric CO₂ concentration and the relative increase in zonally averaged gross primary production (GPP) for 2×CO₂.
28 The observed CO₂ amplitude sensitivities at respective stations provide a constraint on the increase of GPP due to the CO₂
29 fertilization effect, namely $37\% \pm 9\%$ and $32\% \pm 9\%$ for 2×CO₂ in the NHL and the extra-tropical region, respectively.

30
31 Focusing on the NHL, Winkler et al. (2019) investigated how both effects of CO₂ enhance plant productivity while assess-
32 ing the feasibility of vegetation greenness changes as a constraint. Enhanced GPP due to the physiological effect and ensuing
33 climate warming is indirectly evident in large-scale increase in summer time green leaf area (Myneni et al., 1997a; Zhu et al.,
34 2016). Historical CMIP5 simulations show that the maximum annual leaf area index (LAI_{max}, leaf area per ground area) in-
35 creases linearly with both CO₂ concentration and temperature in NHL. In all ESMs, these changes in LAI_{max} strongly correlate

1 to changes in GPP arising from the combined radiative and physiological effects of CO₂ enrichment. Thus, the large variation
2 in modeled historical LAI_{max} responses to the effects of CO₂ linearly maps to variation in ΔGPP at 2×CO₂ in the CMIP5
3 ensemble. This linear relationship in inter-model variations enables the usage of the observed longterm change in LAI_{max} as
4 an EC on ΔGPP at 2×CO₂ in NHL (3.4 ± 0.2 Pg C yr⁻¹ for 2×CO₂; Winkler et al., 2019).

5
6 The robustness of these EC estimates is debated, mainly because the EC approach is susceptible to methodological incon-
7 sistencies. For example, Cox et al. (2013), Wang et al. (2014) and Wenzel et al. (2015) investigated on constraining future
8 terrestrial tropical carbon storage using the same set of models and data. However, they arrived at different EC estimates and
9 divergent conclusions. Some reasons for failure and essential criteria of the EC approach were described previously (Bracegir-
10 dle and Stephenson, 2012b; Klein and Hall, 2015), but this list is far from complete. To account for this gap in the literature,
11 a detailed investigation and description of the EC method in terms of its potential sources of uncertainty and the range of
12 applicability are needed.

13
14 Here, we revisit the study of Winkler et al. (2019) and elaborate on key issues concerning the robustness of the EC method.
15 Uncertainty of the constrained estimate depends on (a) observed predictor and (b) modeled relationship, aside from the
16 goodness-of-fit of the latter (green shading in Fig. 1). As for (a), the source of observations is an obvious first line of in-
17 quiry (Sect. 3.1). Spatial aggregation of data and model simulations introduces uncertainties, as the EC method is applied on
18 large areal values of predictor and predictand. This is the subject of Sect. 3.2. The observed and modeled predictors are from
19 the historical period. The representativeness, duration and match between data and models all introduce an uncertainty related
20 to variations in the temporal domain – these are explored in Sect. 3.3. The yellow shading in Fig. 1 represents the total uncer-
21 tainty on observed predictor from these three fronts. Regarding (b), the modeled linear relation varies (grey shading in Fig. 1)
22 depending on three attributes of the forcing, i.e. CO₂ concentration change, its magnitude, rate and effect (Sect. 3.4 and 3.5).
23 Lessons learned from analyses along these lines are presented in the conclusion section at the end.

24

1 2 Data and Methods

2 2.1 Remotely sensed leaf area index

3 We used the recently updated version (V1) of the leaf area index dataset (LAI3g) developed by (Zhu et al., 2013). It was gen-
4 erated using an artificial neural network (ANN) and the latest version (third generation) of the Global Inventory Modeling and
5 Mapping Studies group (GIMMS) Advanced Very High Resolution Radiometer (AVHRR) normalized difference vegetation
6 index (NDVI) data (NDVI3g). The latter have been corrected for sensor degradation, inter-sensor differences, cloud cover, ob-
7 servational geometry effects due to satellite drift, Rayleigh scattering and stratospheric volcanic aerosols (Pinzon and Tucker,
8 2014). This dataset provides global and year-round LAI observations at 15-day (bi-monthly) temporal resolution and 1/12
9 degree spatial resolution from July 1981 to December 2016. Currently, this is the only available record of such length.

10

11 The quality of previous version (V0) of LAI3g dataset was evaluated through direct comparisons with ground measurements
12 of LAI and indirectly with other satellite-data based LAI products, and also through statistical analysis with climatic variables,
13 such as temperature and precipitation variability (Zhu et al., 2013). The LAI3gV0 dataset (and related fraction vegetation-
14 absorbed photosynthetically active radiation dataset) has been widely used in various studies (Anav et al., 2013; Piao et al.,
15 2014; Poulter et al., 2014; Forkel et al., 2016; Zhu et al., 2016; Mao et al., 2016; Mahowald et al., 2016; Keenan et al., 2016).
16 The new version, LAI3gV1, used in our study is an update of that earlier version.

17

18 We also utilized a more reliable but shorter dataset from the Moderate Resolution Imaging Spectroradiometer (MODIS)
19 aboard the NASA's Terra satellite (Yan et al., 2016a, b). These data are well calibrated, cloud-screened and corrected for at-
20 mospheric effects, especially tropospheric aerosols. The sensor-platform is regularly adjusted to maintain a precise orbit. All
21 algorithms, including the LAI algorithm, are physics-based, well-tested and currently producing sixth generation datasets. The
22 dataset provides global and year-round LAI observations at 16-day (bi-monthly) temporal resolution and 1/20 degree spatial
23 resolution from 2000 to 2016.

24

25 Leaf area index is defined as the one-sided green leaf area per unit ground area in broadleaf canopies and as one-half the
26 green needle surface area in needleleaf canopies in both observational and CMIP5 simulation datasets. It is expressed in units
27 of m^2 green leaf area per m^2 ground area. Leaf area changes can be represented either by changes in annual maximum LAI
28 (LAI_{max} ; Cook and Pau, 2013), or growing season average LAI. In this study, we use the former because of its ease and
29 unambiguity, as the latter requires quantifying the start- and end-dates of the growing season, something that is difficult to
30 do accurately in NHL (Park et al., 2016) with the low resolution model data. Further, LAI_{max} , is less influenced by cloudi-
31 ness and noise; accordingly, it is most useful in investigations of long-term greening and browning trends. The drawback of
32 LAI_{max} , is the saturation effect at high LAI values (Myneni et al., 2002). However, this is less of a problem in high latitudinal
33 ecosystems which are less-densely vegetated compared to tropical regions, with LAI_{max} , values typically in the range of 2 to 3.

34

1 The bi-monthly satellite datasets were merged to a monthly temporal resolution by averaging the two composites in the same
2 month and bi-linearly remapped to the resolution of the applied reanalysis product ($0.5^\circ \times 0.5^\circ$, CRU TS4.01).

3

4 **2.2 Environmental driver variables**

5 We use time series of temperature and CO_2 to derive the observed historical forcing (Sect. 2.4) and climatologies of pre-
6 cipitation and temperature to calculate climatic regimes (Fig. 2). Monthly averages of near-surface air temperature and pre-
7 cipitation are from the latest version of the Climatic Research Unit Timeseries dataset (CRU TS4.01). The global data are
8 gridded to $0.5^\circ \times 0.5^\circ$ resolution (Harris et al., 2014). Global monthly means of atmospheric CO_2 concentration are from
9 the GLOBALVIEW- CO_2 product (obspack_co2_1_GLOBALVIEWplus_v2.1_2016_09_02; for details see [https://doi.org/10.](https://doi.org/10.25925/20190520)
10 [25925/20190520](https://doi.org/10.25925/20190520)) provided by the National Oceanic and Atmospheric Administration / Earth System Research Laboratory
11 (NOAA / ESRL).

12

13 **2.3 Earth system model simulations**

14 We analyzed recent climate-carbon simulations of seven ESMs participating in the fifth phase of the Coupled Model Inter-
15 comparison Project, CMIP (Taylor et al., 2012). The model simulated data were obtained from the Earth System Grid Federa-
16 tion, ESGF (<https://esgf-data.dkrz.de/projects/esgf-dkrz/>). Seven ESMs provide output for the variables of interest (GPP, CO_2 ,
17 LAI, and near-surface air temperature) for simulations titled esmHistorical, RCP4.5, RCP8.5, 1pct CO_2 , esmFixClim1, and
18 esmFdbk1. It is the same set of models analyzed in Wenzel et al. (2016) and Winkler et al. (2019). The individual model setups
19 and components are illustrated in more detail in various studies, such as Arora et al. (2013); Wenzel et al. (2014); Mahowald
20 et al. (2016); Winkler et al. (2019).

21

22 The esmHistorical simulation spanned the period 1850 to 2005 and was driven by observed conditions such as solar forcing,
23 emissions or concentrations of short-lived species and natural and anthropogenic aerosols or their precursors, land use, anthro-
24 pogenic as well as volcanic influences on atmospheric composition. The models are forced by prescribed anthropogenic CO_2
25 emissions, rather than atmospheric CO_2 concentrations.

26

27 Several Representative Concentration Pathways (RCPs) have been formulated describing different trajectories of greenhouse
28 gas emissions, air pollutant production and land use changes for the 21st century. These scenarios have been designed based
29 on projections of human population growth, technological advancement and societal responses (van Vuuren et al., 2011; Tay-
30 lor et al., 2012). We analyzed simulations forced with specified concentrations of a high emissions scenario (RCP8.5) and
31 a medium mitigation scenario (RCP4.5) reaching a radiative forcing level of 8.5 and 4.5 W m^{-2} at the end of the century,
32 respectively. These simulations were initialized with the final state at the end of the historical runs and spanned the period 2006

1 to 2100.

2

3 1pctCO2 is an idealized fully coupled carbon-climate simulation initialized from a steady state of the pre-industrial control
4 run and atmospheric CO₂ concentration prescribed to increase 1% yr⁻¹ until quadrupling of the pre-industrial level. The sim-
5 ulations esmFixClim and esmFdbk aim to disentangle the two carbon cycle feedbacks in response to rising CO₂ analogous
6 to the 1pctCO2 setup: In esmFixClim CO₂-induced climate change is suppressed (i.e. radiation transfer model sees constant
7 pre-industrial CO₂ level), while the carbon cycle responds to increasing CO₂ concentration (*vice versa* for esmFdbk; Taylor
8 et al., 2009, 2012; Arora et al., 2013).

9

10 **2.4 Estimation of greening sensitivities**

11 We largely follow the methodology detailed in Winkler et al. (2019). For both model and observational data, the two-dimensional
12 global fields of LAI and the driver variables are cropped according to different classification schemes (namely, climatic regimes,
13 latitudinal bands and vegetation classes; Olson et al., 2001; Fritz et al., 2015). The aggregated values are area-weighted, aver-
14 aged in space, and temporally reduced to annual estimates dependent on the variable: annual maximum LAI, annual average
15 atmospheric CO₂ concentration, and growing degree days (GDD0, yearly accumulated temperature of days where near-surface
16 air temperature > 0° C).

17

18 We use a standard linear regression model to derive the historical greening sensitivities in models and observations alike (for
19 details see the Methods section *Estimation of historical LAI_{max} sensitivity* in Winkler et al., 2019). On the global scale, LAI_{max}
20 is assumed to be a linear function of atmospheric CO₂ concentration. For the temperature-limited high northern latitudes, we
21 also have to account for warming and include temperature as an additional driver. We do this using GDD0. Through a principal
22 component analysis (PCA) of CO₂ and GDD0 we avoid redundancy from co-linearity between the two driver variables, but
23 retain their underlying time-trend and interannual variability (for details see the Methods section *Dimension reduction using*
24 *principal component analysis* in Winkler et al., 2019). In particular, the PCA is performed on large-scale aggregated values
25 as well as on pixel level to investigate on spatial variations. We only retain the first principal component (denoted ω), which
26 explains a large fraction of the variance in models and observations (for more details see Supplementary Table 1 in Winkler
27 et al., 2019). Figure A1 depicts the temporal development of CO₂ and GDD0 as well as their principal component ω for
28 observations. For the NHL, LAI_{max} is then formulated as a linear function of the proxy driver time series ω (Winkler et al.,
29 2019). The best-fit gradients and associated standard errors of the linear regression model represent the LAI_{max} sensitivities,
30 or greening sensitivities, and their uncertainty estimates, respectively.

31

1 3 Results and Discussion

2 There are two parts to the EC methodology (Fig. 1) – a statistically robust relationship between modeled matching pairs of
3 predictor-predictand values and an observed value of the predictor. The predictors are from a representative historical period.
4 The predictands are modeled changes in a variable of interest at another forcing state of the system (e.g. potential future).
5 The projection of the observed predictor on the modeled relation yields a constrained value of the predictand. A causal basis
6 has to buttress the predictor-predictand relationship, else the EC method may be spurious. For example, meaningful coupling
7 between concurrent changes in GPP and LAI_{max} with increasing atmospheric CO₂ concentration underpins our specific case
8 study in the NHL, i.e. some of the enhanced GPP due to rising CO₂ concentration is invested in additional green leaves by
9 plants (Myneni et al., 1997a; Forkel et al., 2016; Zhu et al., 2016; Mao et al., 2016; Winkler et al., 2019). Supplementary Figure
10 1 in Winkler et al. (2019) illustrates the specifics of the causal link underlying this predictor-predictand relationship. This tight
11 coupling assures an approximately constant ratio of predictand to predictor across the models within the ensemble, thus setting
12 up the potential for deriving an EC estimate. Uncertainty in the constrained estimate depends on the observed predictor and
13 modeled relationship, aside from the goodness-of-fit of the latter (Fig. 1). These are detailed below.

14

15 3.1 Uncertainty in Observed Predictor Due to Data Source

16 We investigate observational uncertainty using LAI data from two different sources, AVHRR (1/12 degree) and MODIS (1/20
17 degree), and spatially aggregating these over broad vegetation classes, latitudinal bands and climatic regimes. The observed
18 large-scale LAI_{max} sensitivities to CO₂ forcing are always positive (greening), irrespective of the source data and the method
19 of aggregation (Fig. 2, Tab. 1). Overall, MODIS based estimates have higher uncertainty because of the shorter length of the
20 data record (17 years). The failure to reliably estimate sensitivities in tropical forests (also in the latitudinal band 30° S – 30°
21 N, and in hot, wet and humid climatic regimes, see Tab. 1 and Fig. 2) is due to saturation of optical remote sensing data over
22 dense vegetation (LAI_{max} > 5) and problems associated with high aerosol content and ubiquitous cloudiness. In other regions,
23 the estimated sensitivities are comparable across sensors and aggregation schemes, in particular in the high latitudinal band (>
24 60° N/S; AVHRR: $[3.4 \pm 0.5] \times 10^{-3}$, MODIS: $[3.6 \pm 0.9] \times 10^{-3} \text{ m}^2 \text{ m}^{-2} \text{ ppm}^{-1} \text{ CO}_2$). This aligns with previous studies
25 reporting a net increase in green leaf area across the high latitudes during the observational period (Myneni et al., 1997b; Zhu
26 et al., 2016; Forkel et al., 2016).

27

28 This analysis illustrates the applicability and limitations of using observed greening sensitivities to CO₂ forcing as a con-
29 straint on photosynthetic production. For example, data from both AVHRR and MODIS sensors provide a comparable estimate
30 of greening sensitivity in the colder high latitudes (boreal forests and tundra vegetation classes; Winkler et al., 2019). In the
31 lower latitudes, however, the discrepancies among the two sensors indicate a considerable observational uncertainty and thus
32 no robust estimation of the observed predictor is possible.

33

1 3.2 Uncertainty Due to Spatial Aggregation

2 We focus further analyses on the NHL region ($> 60^\circ$ N; Fig. 2b), because of two reasons. First, the direct human impact (i.e.
3 land management) can be neglected in the high latitudes, thus, we can assume that the observed changes reflect the response of
4 natural ecosystems. Second, the observational evidence of an increased plant productivity in the recent decades is well estab-
5 lished (e.g. Keeling et al., 1996; Myneni et al., 1997a; Graven et al., 2013; Forkel et al., 2016; Wenzel et al., 2016, and Sect.
6 3.1) – an important requisite in defining a robust predictor.

7

8 In addition to the physiological effect of CO_2 , warming also plays a key role in controlling plant productivity of the NHL
9 temperature-limited ecosystems, and thus, vegetation greenness. To avoid redundancy from co-linearity between CO_2 and
10 GDD0, we reduce dimensionality by performing a principal component analysis of the two driver variables (Sect. 2.4). The
11 resulting first principal component explains most of the variance and retains the trend and year-to-year fluctuations in both
12 CO_2 and GDD0. Therefore, we obtain a proxy driver (hereafter denoted ω) that represents the overall forcing signal causing
13 observed vegetation greenness changes in NHL (Fig. A1). Accordingly, greening sensitivity for the entire NHL area is derived
14 as response to ω , the combined forcing signal of rising CO_2 and warming. This procedure also enables a better comparability
15 between observations and models because varying strengths of physiological and radiative effects of CO_2 among models are
16 taken into account (Sect. 3.3 – 3.5).

17

18 The vegetated landscape in the NHL region is heterogeneous, with boreal forests in the south, vast tundra grasslands to the
19 north and shrublands in-between. The species within each of these broad vegetation classes respond differently to changes in
20 key environmental factors. Even within a species, such responses might vary due to different boundary conditions, such as
21 topography, soil fertility, micrometeorological conditions, etc. How this fine scale variation in greening sensitivity impacts the
22 aggregated value is assessed below.

23

24 The distribution of greening sensitivities from all NHL pixels is slightly skewed towards the positive (blue histogram). The
25 mean value of this distribution (blue dashed line) is comparable to the sensitivity estimate derived from the spatially-averaged
26 NHL time series (yellow dashed line; Fig. 3). Based on the Mann-Kendall test ($p > 0.1$), nearly over half the pixels (54%) show
27 positive statistically significant trends (greening), while about 10% show browning trends (possibly due to disturbances; Goetz
28 et al., 2005). The distribution of these statistically significant sensitivities (red histogram) therefore has two modes, a weak
29 browning and a dominant greening mode, resulting in a substantially higher mean value (red dashed line) in comparison to the
30 spatially-averaged estimate (yellow dashed line; Fig. 3). Thus, by taking into account the remaining 36% of non-significantly
31 changing pixels (as in the NHL spatially-averaged estimate), an additional source of uncertainty is possibly introduced. The
32 mean sensitivity value is, of course, higher when only pixels showing a greening trend are considered in the analysis (green
33 dashed line; Fig. 3). These are the only areas in NHL that actually show a large increase in plant productivity and consequently

1 significant changes in leaf area.

2

3 Model output of several ESMs (CMIP5) reveal similar pixel-level variation in both the predictor (LAI_{max} to ω , historical
4 simulation; Sect. 2.3) and associated changes in the predictand (GPP, 1pctCO₂; Sect. 2.3), although ESMs operate on much
5 coarser resolution (Fig. A2; see also Anav et al., 2013, 2015). Due to the coupling of the predictor and predictand, the distri-
6 bution of pixels with significant changes is approximately the same for the two variables (Fig. A2). Accordingly, averaging
7 the equally distributed estimates likely does not affect the predictor-predictand relationship in the model ensemble (Fig. 1).
8 Consequently, if all spatial gridded data arrays are consistently processed to spatially-aggregated estimates, each predictand
9 and predictor (observed and modeled) estimate contain a coherent component of spatial variations. In other words, considering
10 browning and non-significant pixels results in a lower overall LAI_{max} sensitivity in NHL, which in turn leads to a lower con-
11 strained estimate of ΔGPP in NHL. This is consistent with the underlying relationship between predictor and predictand. On a
12 related note, Bracegirdle and Stephenson (2012a) suggest that this source of error is not significantly dependent on the spatial
13 resolution when comparing model subsets from high to low resolution.

14

15 The above analysis informs that spatially-averaged estimates are approximations containing a random error component due
16 to inclusion of data from insignificantly changing pixels and a systematic bias component from pixels of reversed sign. This
17 uncertainty is relevant to the EC method, where the observed sensitivity decisively determines the constrained estimate from
18 the ensemble of ESM projections (Kwiatkowski et al., 2017; Winkler et al., 2019). However, if spatial variations are treated
19 consistently as an inherent component of observations and models, the EC method is only slightly susceptible to this source of
20 uncertainty.

21

22 3.3 Uncertainty Due to Temporal Variations

23 We seek recourse to longterm CMIP5 ESM simulations covering the historical period 1850 to 2005 (Sect. 2.3) to assess
24 temporal variation in the predictor variable, because of the shortness of observational record. Three representative models
25 (CESM1-BGC, MIROC-ESM, and HadGEM2-ES) spanning the full range of NHL greening sensitivities in the CMIP5 en-
26 semble (Winkler et al., 2019) are selected for this analysis. For each model, LAI_{max} sensitivity to ω in moving windows of
27 different lengths are evaluated (15, 30, and 45 years; Fig. 4 and A3). The analysis reveals two crucial aspects that highlight how
28 temporal variations impair comparability of the predictor variable between models and observations – an essential component
29 of the EC approach.

30

31 First, window locations of modeled and observed predictor variable have to match. If the forcing in the simulations is low,
32 for example, as in the second half of the 19th century when CO₂ concentration was increasing slowly, inter-annual variability
33 dominates and LAI_{max} sensitivity cannot be accurately estimated irrespective of the window length (Fig. 4 and A3). With in-
34 creasing forcing over time (rising yearly rate of CO₂ emissions, and consequently, the concentration), the signal-to-noise ratio

1 increases and LAI_{\max} sensitivity to ω estimation stabilizes, for example, as in the second half of the 20th century. Therefore,
2 LAI_{\max} sensitivities estimated at different temporal locations result in non-comparable values and eventually a false con-
3 strained estimate (details in Sect. 3.4). As an example, modeled sensitivities based on a 30-year window centered on year 1900,
4 when CO_2 level increased by 10 ppm, and observed sensitivity estimated from a 30-year window centered on year 2000, when
5 CO_2 level increased by 55 ppm, describe different states of the system and therefore should not be contrasted in the EC method.

6
7 Second, in addition to temporal location, also window lengths have to match between observations and models. For all three
8 models, sensitivities estimated from 15-year chunks show high variability and thus, a 15-year record is perhaps too short to
9 obtain robust estimates. The LAI_{\max} sensitivity estimation becomes more stable with strengthening forcing and increasing
10 window length (Fig. 4 and A3). As a consequence, using short-term observed sensitivity as a constraint on long-term model
11 projections results in an incorrect EC estimate. Hence, the MODIS sensor record is, on the one hand, too short and does not,
12 on the other hand, overlap temporally with the historical CMIP5 forcing. Therefore, it does not provide a robust predictor in
13 this EC study.

14 3.4 Level and Time Rate of CO_2 Forcing

15 The EC method raises an obvious question – does it not implicitly assume that the key operative mechanisms underpinning the
16 EC relation remain unchanged because a future system state is being predicted based on its past behavior? To be specific, we
17 are attempting to predict GPP at a future point in time based on greening sensitivity inferred from the past. Does this not require
18 the assumption that the key underlying relationship which makes this prediction possible, namely, a robust coupling between
19 contemporaneous changes in GPP and LAI_{\max} remains unchanged from the past to the future? To address this question, we
20 resort to the CMIP5 idealized simulation (1pctCO2), where atmospheric CO_2 concentration increases 1% annually, starting
21 from a pre-industrial level of 284 ppm until a quadruple of this value is reached (Sect. 2.3). We limit the analysis to the three
22 models (CESM1-BGC, MIROC-ESM, and HadGEM2-ES) which bracket the full range of GPP enhancement and LAI_{\max}
23 sensitivity in the original seven ESM ensemble (Winkler et al., 2019).

24
25
26 The relationship between simultaneous changes in GPP and LAI_{\max} remains linear for all CMIP5 models in the range
27 $1 \times CO_2$ to $2 \times CO_2$ (Fig. 5 and A4, Tab. 2). With concentration increasing beyond $2 \times CO_2$, all models show weakening correla-
28 tion (R^2 , Tab. 2) and decreasing slope (b , Tab. 2) of this relationship (Fig. 5 and A4), suggesting a saturating rate of allocation
29 of additional GPP to new leaves at higher levels of CO_2 . Consequently, LAI_{\max} sensitivity to increasing CO_2 and associated
30 warming decreases. At and over $4 \times CO_2$ (1140 ppm), a level unlikely to be seen in the near future, there appears to be no
31 relationship between ΔGPP and ΔLAI_{\max} in some models. This raises the question as to what extent does the weakening of
32 the relationship between the predictor and predictand in each model at higher CO_2 concentrations affect the EC analysis (Fig.
33 1). To shed light on this matter, we perform the following thought experiment.

34

1 Understanding the relationship and interplay between forcing (increasing CO₂ concentration), predictor (LAI_{max} sensitiv-
2 ity), and the predictand (Δ GPP) is key to evaluating the EC method. We conceive four possible scenarios of how the sys-
3 tem might behave with increasing forcing. For simplicity, we assume linearly increasing CO₂ concentration, LAI represents
4 LAI_{max}, and GPP refers to its annual value below (Fig. 6). The four scenarios are: *All linear*, *all non-linear* (saturation), and
5 two *mixed linear / non-linear* cases (Tab. A1). We emulate a multi-model ensemble by applying different random parameteri-
6 zations for the linear and saturation (the hyperbolic tangent function) responses of GPP to CO₂ and of LAI to GPP. One of these
7 realizations is assumed to represent pseudo-observations (dashed lines, Fig. 6). We discuss one case in detail for illustrative
8 purposes (No. 3, Tab. A1).

9
10 In scenario 3, Δ GPP increases linearly with increasing CO₂ (Fig. 6a), while Δ LAI/ Δ GPP saturates (Fig. 6b). The LAI sen-
11 sitivity to CO₂ weakens with increasing forcing (Fig. 6c) as a response to saturation of GPP allocation to leaf area. We derive
12 LAI sensitivities to CO₂ for three different periods ('past periods' in Fig. 6c) to constrain Δ GPP at a much higher CO₂ level
13 ('projected period' in Fig. 6a). Next, we apply the EC method on these pseudo-projections of Δ GPP relying on LAI sensitivi-
14 ties derived from the three past periods (Fig. 6d). The EC method is applicable even at a low forcing level (past period 1) in this
15 simplified scenario because we neglect stochastic internal variability of the system. The slope of emergent linear relationship
16 increases (Fig. 6d) as modeled LAI sensitivities decrease with rising CO₂ concentration (Fig. 6c). The observational constraint
17 on future Δ GPP, however, remains nearly the same, because pseudo-observed LAI sensitivity also weakens at higher CO₂
18 levels (dashed lines, Fig. 6c, d). Thus, the three EC estimates of Δ GPP are approximately identical (Fig. 6d) and independent
19 of the forcing level during past periods. With intensified forcing, the relationship between predictor and predictand remains
20 linear within the model ensemble, although their relationship becomes non-linear within each model and, crucially, in reality
21 as well. In other words, as long as the models agree on the occurrence and strength of saturation for given forcing, i.e. the
22 dynamics of the system, the inter-model variations of predictor and predictand relate linearly within the ensemble (Fig. 6). The
23 same behavior is also seen in the other three scenarios (Tab. A1; Fig. A5, A6).

24
25 Nevertheless, with ever increasing forcing and associated steepening of the emergent linear relationship, the LAI sensitivity
26 loses its explanatory power at some point because the linear relationship eventually lies within the observational uncertainty
27 and no meaningful constraint can be derived. This and disagreement between models on system dynamics are ultimate limits
28 of the EC method. Interestingly, we find that all CMIP5 models agree on the occurrence of saturation, but slightly disagree on
29 the strength of saturation for given CO₂ forcing (Fig. 5, A4, and Tab. 2). Further, we find that the 'all non-linear' scenario best
30 describes the dynamics of the system in the forcing range from 1×CO₂ to 4×CO₂. However, the saturation of LAI to GPP
31 happens at a lower CO₂ level than saturation of GPP to CO₂. Still, inferences from interpretation of Case 3 (Fig. 6) are equally
32 applicable.

33
34 Results from the above thought experiment also highlight the importance of matching window locations and lengths between
35 models and observations, as discussed earlier (Sect. 3.3). For instance, taking LAI sensitivity from past period 2 (green dashed

1 line, Fig. 6d) as an observational constraint on the multi-model linear relationship based on past period 3 (red solid line, Fig.
2 6d), results in a significant overestimation of constrained ΔGPP (intersection of the two lines, Fig. 6d).

3
4 The above analysis informs that the constrained GPP estimate at one future period (e.g. $2\times\text{CO}_2$) is nearly independent of
5 the past periods from when the observational sensitivities are derived. Now, we evaluate the EC method where sensitivity from
6 one past period is used to obtain constrained GPP estimates at different periods in a potential future, i.e. progressively farther
7 down the time-line of a CO_2 -enriched world. We utilize the greening sensitivity derived from 35 years of observed LAI_{max}
8 data (AVHRR, Sect. 2.1) and apply the EC method to CMIP5 1pctCO2 simulations. The sensitivities in this case are due to
9 forcing from both CO_2 increase and associated warming during the observational period (Sect. 2.4). We seek constrained GPP
10 estimates for the NHL at different CO_2 levels ($2\times\text{CO}_2$, $3\times\text{CO}_2$, and $4\times\text{CO}_2$).

11
12 Winkler et al. (2019) previously reported a strong linear relationship between modeled contemporaneous changes in LAI_{max}
13 and GPP arising from the combined radiative and physiological effects of CO_2 enrichment until $2\times\text{CO}_2$ in the CMIP5 ensem-
14 ble. As a result, models with low LAI_{max} sensitivity to ω project lower ΔGPP for a given increment of CO_2 concentration, and
15 *vice versa*. Thus, the large variation in modeled historical LAI_{max} sensitivities linearly maps to variation in ΔGPP at $2\times\text{CO}_2$
16 (Winkler et al., 2019, blue line, Fig. 7a). At higher levels, such as $3\times\text{CO}_2$ (green line, $R^2 = 0.93$) and $4\times\text{CO}_2$ (red line, R^2
17 $= 0.88$), this linear relationship within the model ensemble, while still present, weakens (Fig. 7a; Tab. 3). This is because the
18 CMIP5 models do not agree on the strength of the saturation effect at higher CO_2 levels (Fig. 5 and A4). The increment in
19 constrained GPP estimates for successive equal increments of CO_2 decreases due to the saturation effect in all CMIP5 models
20 (dashed horizontal lines, Fig. 7a). For example, the change in GPP between $3\times\text{CO}_2$ and $4\times\text{CO}_2$ ($\Delta\text{GPP} \sim 1.06 \text{ Pg C yr}^{-1}$,
21 Tab. 3) is much lower than between $2\times\text{CO}_2$ and $3\times\text{CO}_2$ ($\Delta\text{GPP} \sim 2.34 \text{ Pg C yr}^{-1}$, Tab. 3).

22
23 We have thus far focused on the magnitude of CO_2 concentration change and not on the time rate of this change. For example,
24 a given amount of change in CO_2 concentration, say 200 ppm, can be realized over different time periods, say over a 100 or 150
25 years. The problem of varying rates of CO_2 concentration change is implicitly encountered when ESMs are executed under
26 different forcing scenarios, such as RCPs (Sect. 2.3). A question then arises whether the constrained predictand estimate is
27 independent of the time rate of CO_2 concentration change and dependent only on the magnitude of CO_2 concentration change.
28 To investigate this aspect of forcing, we extract GPP estimates at the same CO_2 concentration (535 ppm; final concentration
29 in RCP4.5) from three simulations of different forcing rates and calculate the difference relative to a common initial CO_2
30 concentration (380 ppm; initial concentration of RCP scenarios). Hence, the magnitude of the forcing is the same but applied
31 over different durations (RCP4.5: $\sim 90\text{yr}$, RCP8.5: $\sim 45\text{yr}$, and 1pctCO2: $\sim 30\text{yr}$). A clear majority of the CMIP5 models show
32 substantial differences in ΔGPP between the different pathways of CO_2 forcing. In general, GPP changes are higher for lower
33 time rates of CO_2 forcing, i.e. forcing over longer time periods. As a consequence, the EC estimates of ΔGPP for the same
34 increase in CO_2 concentration are scenario-dependent (Fig. 7b; Tab. 3) – a counter-intuitive result. For instance, the low- CO_2 -
35 rate scenario RCP4.5 shows the largest GPP enhancement ($\Delta\text{GPP} \sim 2.84 \text{ Pg C yr}^{-1}$, Tab. 3) for an increase of 155 ppm CO_2 .

1 This estimates is $\sim 39\%$ and $\sim 20\%$ larger than in the scenarios with higher CO_2 rates for the same total increment in CO_2
2 concentration, namely 1pctCO2 ($\Delta\text{GPP} \sim 2.05 \text{ Pg C yr}^{-1}$, Tab. 3) and RCP8.5 ($\Delta\text{GPP} \sim 2.38 \text{ Pg C yr}^{-1}$, Tab. 3), respectively.
3 This analysis suggests that the vegetation response to rising CO_2 is pathway dependent, at least in the NHL. One of the reasons
4 for this could be species compositional changes in scenarios of low forcing rates, i.e. over longer time frames. This novel result,
5 however, requires a separate in-depth study.

6 **3.5 Effects of CO_2 Forcing**

7 Higher concentration of CO_2 in the atmosphere stimulates plant productivity through the fertilization and radiative effects (Ne-
8 mani et al., 2003; Leakey et al., 2009; Arora et al., 2011; Goll et al., 2017). The two effects can be disentangled in the model
9 world by conducting simulations in a 'CO₂ fertilization effect only' (esmFixClim1) and a 'radiative effect only' (esmFdbk1)
10 setup (Sect. 2.3). These are termed below as idealized model simulations. We investigate here whether historical runs and
11 observations, which include both effects, can be used to constrain GPP changes in idealized CMIP5 simulations (e.g. as in
12 Wenzel et al., 2016).

13

14 We find strong linear relationships between historical LAI_{max} sensitivity and ΔGPP for $2\times\text{CO}_2$ in both idealized setups
15 (esmFixClim1: $R^2 = 0.92$, esmFdbk1: $R^2 = 0.98$, Tab. 3, Fig. 7c). Consequently, this linear relationship is also pronounced for
16 calculated sums of both effects for each model (esmFixClim1 + esmFdbk1: $R^2 = 0.95$, Tab. 3, Fig. 7c). This suggests that the
17 two effects act additively on plant productivity and, thus, each effect can be simply expressed in terms of a scaling factor of
18 the total GPP enhancement. Hence, the application of the EC method on idealized simulations using real world observations is
19 conceptually feasible.

20

21 Interestingly, the two effects contribute about the same to the general increase in GPP at $2\times\text{CO}_2$ (esmFixClim1: ΔGPP
22 $\sim 1.35 \text{ Pg C yr}^{-1}$, esmFdbk1: $\Delta\text{GPP} \sim 1.38 \text{ Pg C yr}^{-1}$, Tab. 3, Fig. 7c). At higher concentrations, such as $3\times\text{CO}_2$ and $4\times\text{CO}_2$,
23 the enhancement in GPP saturates in both idealized setups. However, the radiative effect becomes dominant relative to the
24 CO_2 fertilization effect when CO_2 concentration exceeds $2\times\text{CO}_2$ (e.g. at $4\times\text{CO}_2$ esmFixClim1: $\Delta\text{GPP} \sim 2.42 \text{ Pg C yr}^{-1}$,
25 esmFdbk1: $\Delta\text{GPP} \sim 3.06 \text{ Pg C yr}^{-1}$, Tab. 3). Therefore, we can expect that at some point in the future, NHL photosynthetic
26 carbon fixation will benefit more from climate change (e.g. warming) than from the fertilizing effect of CO_2 .

27 **3.6 Uncertainties in the Multi-Model Ensemble**

28 Besides methodological sources of uncertainty discussed above, the estimate of an EC may also be deficient due to inaccurate
29 assumptions about the model ensemble. First, possible common systematic errors in a multi-model ensemble (i.e. the entire
30 ensemble misses an unknown process, which plays a key role in a high CO_2 world) are implicitly omitted in the EC ap-
31 proach, however, could cause a general over- or underestimation of the constrained value (Bracegirdle and Stephenson, 2012b;
32 Stephenson et al., 2012). Second, the set of forcing variables for historical simulations may be incomplete (i.e. not yet identified
33 drivers of observed changes) and thus the comparability of observations and model simulations is limited (Flato et al., 2013).

1 Third, the EC method can be overly sensitive to individual models of the ensemble, which has a bearing on the robustness of
2 the constrained value (Bracegirdle and Stephenson, 2012b). Bracegirdle and Stephenson (2012b) proposed a diagnostic metric
3 (Cook's distance) to test an ensemble for influential models. Fourth, the predictand-predictor relationship not only has to rely
4 on a physical, but also on a logical connection within the model ensemble. For instance, Wenzel et al. (2016) established a
5 linear relationship between relative changes in the predictand taking the initial state into account (changes in GPP for doubling
6 of CO₂ relative to the initial pre-industrial state), and a predictor neglecting the initial state (historical sensitivity of CO₂ am-
7 plitude to rising CO₂). This statistical relationship can be spurious, because the model skill of simulating an accurate initial
8 state and a plausible sensitivity to a forcing are not connected. These issues are to be contemplated when establishing an EC
9 estimate and evaluating its robustness.

10 **4 Conclusions**

11 An in-depth analysis of the EC method is illustrated in this article through its application to projections of change in NHL
12 photosynthesis under conditions of rising atmospheric CO₂ concentration. Key conclusions highlighting the functionality of
13 the EC method are presented below.

14

15 The importance of how the observational predictor is obtained cannot be emphasized enough because the EC method is
16 particularly sensitive to observational uncertainty. The single observational estimate essentially determines the EC, whereas
17 the emergent linear relationship is established based on a collection of multi-model estimates (each model gets 'one vote',
18 however, some models might be more influential than others; Bracegirdle and Stephenson, 2012b). Hence, the observational
19 uncertainty has a much larger bearing on the EC than the uncertainty of each individual model. To overcome this source of
20 uncertainty, various meaningful observations should be taken into consideration when establishing the observed predictor.

21

22 Spatially aggregating observations and model output of different resolutions in the EC method constitutes another source
23 of uncertainty. Predictors and predictands expressed as regional estimates (e.g. area-weighted mean of the NHL) are approxi-
24 mations of complex fine-scale processes. Aggregation will inevitably introduce a random error component due to inclusion of
25 estimates from areas where the predictor is not changing or a systematic bias from areas where the predictor has a reversed
26 sign. Thus, the spatially-aggregated variables are meaningful only if most of the region is in agreement about the response to
27 CO₂ forcing (e.g. more than half of the NHL is greening with rising CO₂). However, we find that the source of uncertainty
28 related to spatial aggregation is of minor importance as long as spatial variations in observations and models simulations are
29 treated consistently.

30

31 A large source of uncertainty is associated with temporal variability of the predictor variable when comparing models and
32 observations. Establishing a robust predictor requires evaluating temporal window lengths of sufficient duration (approximately
33 30 years) and their locations along the forcing time line. Both window length and location should match between models and

1 observations in the EC method. For example, the analysis in Wenzel et al. (2016) might have yielded different results and
2 conclusions if model and observational predictor sensitivities were temporally matched. We find that the relevance of window
3 length decreases with increasing and accelerating forcing, depending on the magnitude of natural/internal variability (signal-
4 to-noise ratio) of the predictor variable.

5
6 The level, effect and time-rate of applied CO₂ forcing can have a bearing on the linear relationship between the predictand
7 and predictor variables (Fig. 1). In our case study, the relationship underpinning the EC method, namely, that between concur-
8 rent ΔGPP and $\Delta\text{LAI}_{\text{max}}$ changes non-linearly with increasing forcing level (i.e. saturation with rising CO₂ concentration).
9 The EC method can still be applied, because the CMIP5 models agree on the non-linear behavior of the system. However,
10 at very high CO₂ concentrations the models diverge and this relation breaks down, at which point the EC method fails. The
11 two dominant effects of rising CO₂ concentration on vegetation, namely, the fertilization and radiative effects, appear to be
12 approximately additive in terms of GPP enhancement to CO₂ forcing in the NHL. Therefore, the EC method can be applied to
13 constrain estimates of GPP due to one or the other, or both the effects. The models, however, document a higher radiative effect
14 than fertilization at concentrations exceeding $2\times\text{CO}_2$. Another intriguing conclusion from our analysis is that the time-rate of
15 forcing has an effect on GPP changes, that is, the projected GPP enhancement to CO₂ forcing seems to be dependent on how
16 the forcing is applied over time, as in different scenarios or RCPs. This aspect is presently not well understood and requires
17 further study.

18
19 The EC framework is widely promoted as observation-based evaluation tool for climate projections, especially in the context
20 of the nascent CMIP6 ensemble (Eyring et al., 2019; Hall et al., 2019). Previous EC studies, however, exclusively focused on
21 predictor-predictand combinations which exhibit so-called existent ECs (Hall et al., 2019), i.e. predictor and predictand are
22 found to relate linearly across the ensemble. In the context of ESM evaluation, non-existent ECs, i.e. predictor and predictand
23 are found to be unrelated in the ensemble, are equally important. Since predictor and predictand variables are premised on
24 our mechanistic process understanding, non-existent ECs reveal a fundamental disagreement on the system dynamics among
25 the models. This study encourages to scrutinize these system dynamics in the predictor-predictand space and also report such
26 non-existent, yet expected, ECs in order to advance model development and evaluation.

27
28 Across different disciplines each EC and its set of predictor and predictand are unique to some extent and require an individ-
29 ual detailed examination. In this article, we addressed general potential sources of uncertainty and limitations in the EC method
30 by the means of a case study in carbon cycle research. Thus, the illustrated results are qualitatively transmissive to other sets
31 of predictors and predictands and are generally relevant in Earth system sciences.

1 *Author contributions.* A.J.W. performed the analysis. All authors contributed ideas and to writing of the manuscript.

2 *Competing interests.* The authors declare that they have no conflict of interest.

3 *Acknowledgements.* We thankfully acknowledge T. Park and C. Chen for their help with remote sensing data. We thank G. Lasslop for
4 reviewing the manuscript. R.B.M. thanks Alexander von Humboldt Foundation and NASA's Earth Science Division for funding support that
5 made his participation possible in this research. Finally, we thank three anonymous reviewers and Vivek Arora whose comments helped to
6 substantially improve the manuscript.

1 **References**

- 2 Anav, A., Friedlingstein, P., Kidston, M., Bopp, L., Ciais, P., Cox, P., Jones, C., Jung, M., Myneni, R., and Zhu, Z.: Evaluating the
3 Land and Ocean Components of the Global Carbon Cycle in the CMIP5 Earth System Models, *Journal of Climate*, 26, 6801–6843,
4 <https://doi.org/10.1175/JCLI-D-12-00417.1>, 2013.
- 5 Anav, A., Friedlingstein, P., Beer, C., Ciais, P., Harper, A., Jones, C., Murray-Tortarolo, G., Papale, D., Parazoo, N. C., Peylin, P., Piao, S.,
6 Sitch, S., Viovy, N., Wiltshire, A., and Zhao, M.: Spatiotemporal Patterns of Terrestrial Gross Primary Production: A Review, *Reviews of*
7 *Geophysics*, 53, 2015RG000483, <https://doi.org/10.1002/2015RG000483>, 2015.
- 8 Arora, V. K., Scinocca, J. F., Boer, G. J., Christian, J. R., Denman, K. L., Flato, G. M., Kharin, V. V., Lee, W. G., and Merryfield, W. J.:
9 Carbon Emission Limits Required to Satisfy Future Representative Concentration Pathways of Greenhouse Gases, *Geophysical Research*
10 *Letters*, 38, L05 805, <https://doi.org/10.1029/2010GL046270>, 2011.
- 11 Arora, V. K., Boer, G. J., Friedlingstein, P., Eby, M., Jones, C. D., Christian, J. R., Bonan, G., Bopp, L., Brovkin, V., Cadule, P., Hajima, T.,
12 Ilyina, T., Lindsay, K., Tjiputra, J. F., and Wu, T.: Carbon–Concentration and Carbon–Climate Feedbacks in CMIP5 Earth System Models,
13 *Journal of Climate*, 26, 5289–5314, <https://doi.org/10.1175/JCLI-D-12-00494.1>, 2013.
- 14 Boé, J., Hall, A., and Qu, X.: September Sea-Ice Cover in the Arctic Ocean Projected to Vanish by 2100, *Nature Geoscience*, 2, 341–343,
15 <https://doi.org/10.1038/ngeo467>, 2009.
- 16 Bracegirdle, T. J. and Stephenson, D. B.: Higher Precision Estimates of Regional Polar Warming by Ensemble Regression of Climate Model
17 Projections, *Climate Dynamics*, 39, 2805–2821, <https://doi.org/10.1007/s00382-012-1330-3>, 2012a.
- 18 Bracegirdle, T. J. and Stephenson, D. B.: On the Robustness of Emergent Constraints Used in Multimodel Climate Change Projections of
19 Arctic Warming, *Journal of Climate*, 26, 669–678, <https://doi.org/10.1175/JCLI-D-12-00537.1>, 2012b.
- 20 Cook, B. I. and Pau, S.: A Global Assessment of Long-Term Greening and Browning Trends in Pasture Lands Using the GIMMS LAI3g
21 Dataset, *Remote Sensing*, 5, 2492–2512, <https://doi.org/10.3390/rs5052492>, 2013.
- 22 Cox, P. M., Pearson, D., Booth, B. B., Friedlingstein, P., Huntingford, C., Jones, C. D., and Luke, C. M.: Sensitivity of Tropical Carbon to
23 Climate Change Constrained by Carbon Dioxide Variability, *Nature*, 494, 341–344, <https://doi.org/10.1038/nature11882>, 2013.
- 24 Cox, P. M., Huntingford, C., and Williamson, M. S.: Emergent Constraint on Equilibrium Climate Sensitivity from Global Temperature
25 Variability, *Nature*, 553, 319–322, <https://doi.org/10.1038/nature25450>, 2018.
- 26 Eyring, V., Bony, S., Meehl, G. A., Senior, C. A., Stevens, B., Stouffer, R. J., and Taylor, K. E.: Overview of the Coupled Model Intercompar-
27 ison Project Phase 6 (CMIP6) Experimental Design and Organization, *Geosci. Model Dev.*, 9, 1937–1958, [https://doi.org/10.5194/gmd-](https://doi.org/10.5194/gmd-9-1937-2016)
28 [9-1937-2016](https://doi.org/10.5194/gmd-9-1937-2016), 2016.
- 29 Eyring, V., Cox, P. M., Flato, G. M., Gleckler, P. J., Abramowitz, G., Caldwell, P., Collins, W. D., Gier, B. K., Hall, A. D., Hoffman, F. M.,
30 Hurtt, G. C., Jahn, A., Jones, C. D., Klein, S. A., Krasting, J. P., Kwiatkowski, L., Lorenz, R., Maloney, E., Meehl, G. A., Pendergrass,
31 A. G., Pincus, R., Ruane, A. C., Russell, J. L., Sanderson, B. M., Santer, B. D., Sherwood, S. C., Simpson, I. R., Stouffer, R. J., and
32 Williamson, M. S.: Taking Climate Model Evaluation to the next Level, *Nature Climate Change*, p. 1, [https://doi.org/10.1038/s41558-018-](https://doi.org/10.1038/s41558-018-0355-y)
33 [0355-y](https://doi.org/10.1038/s41558-018-0355-y), 2019.
- 34 Flato, G., Marotzke, J., Abiodun, B., Braconnot, P., Chou, S., Collins, W., Cox, P., Driouech, F., Emori, S., Eyring, V., Forest, C., Gleckler,
35 P., Guilyardi, E., Jakob, C., Kattsov, V., Reason, C., and Rummukainen, M.: Evaluation of Climate Models, in: *Climate Change 2013:*
36 *The Physical Science Basis. Contribution of Working Group I to the Fifth Assessment Report of the Intergovernmental Panel on Climate*

1 Change, edited by Stocker, T., Qin, D., Plattner, G.-K., Tignor, M., Allen, S., Boschung, J., Nauels, A., Xia, Y., Bex, V., and Midgley, P.,
2 pp. 741–866, Cambridge University Press, Cambridge, United Kingdom and New York, NY, USA, 2013.

3 Forkel, M., Carvalhais, N., Rödenbeck, C., Keeling, R., Heimann, M., Thonicke, K., Zaehle, S., and Reichstein, M.: En-
4 hanced Seasonal CO₂ Exchange Caused by Amplified Plant Productivity in Northern Ecosystems, *Science*, 351, 696–699,
5 <https://doi.org/10.1126/science.aac4971>, 2016.

6 Fritz, S., See, L., McCallum, I., You, L., Bun, A., Moltchanova, E., Duerauer, M., Albrecht, F., Schill, C., Perger, C., Havlik, P., Mosnier, A.,
7 Thornton, P., Wood-Sichra, U., Herrero, M., Becker-Reshef, I., Justice, C., Hansen, M., Gong, P., Abdel Aziz, S., Cipriani, A., Cumani,
8 R., Cecchi, G., Conchedda, G., Ferreira, S., Gomez, A., Haffani, M., Kayitakire, F., Malanding, J., Mueller, R., Newby, T., Nonguierma,
9 A., Olusegun, A., Ortner, S., Rajak, D. R., Rocha, J., Schepaschenko, D., Schepaschenko, M., Terekhov, A., Tiangwa, A., Vancutsem, C.,
10 Vintrou, E., Wenbin, W., van der Velde, M., Dunwoody, A., Kraxner, F., and Obersteiner, M.: Mapping Global Cropland and Field Size,
11 *Global Change Biology*, 21, 1980–1992, <https://doi.org/10.1111/GCB.12838>, 2015.

12 Goetz, S. J., Bunn, A. G., Fiske, G. J., and Houghton, R. A.: Satellite-Observed Photosynthetic Trends across Boreal North America As-
13 sociated with Climate and Fire Disturbance, *Proceedings of the National Academy of Sciences of the United States of America*, 102,
14 13 521–13 525, <https://doi.org/10.1073/pnas.0506179102>, 2005.

15 Goll, D. S., Winkler, A. J., Raddatz, T., Dong, N., Prentice, I. C., Ciais, P., and Brovkin, V.: Carbon–Nitrogen Interactions in Idealized
16 Simulations with JSBACH (Version 3.10), *Geosci. Model Dev.*, 10, 2009–2030, <https://doi.org/10.5194/gmd-10-2009-2017>, 2017.

17 Graven, H. D., Keeling, R. F., Piper, S. C., Patra, P. K., Stephens, B. B., Wofsy, S. C., Welp, L. R., Sweeney, C., Tans, P. P., Kelley, J. J.,
18 Daube, B. C., Kort, E. A., Santoni, G. W., and Bent, J. D.: Enhanced Seasonal Exchange of CO₂ by Northern Ecosystems Since 1960,
19 *Science*, 341, 1085–1089, <https://doi.org/10.1126/science.1239207>, 2013.

20 Hall, A. and Qu, X.: Using the Current Seasonal Cycle to Constrain Snow Albedo Feedback in Future Climate Change, *Geophysical Research*
21 *Letters*, 33, L03 502, <https://doi.org/10.1029/2005GL025127>, 2006.

22 Hall, A., Cox, P., Huntingford, C., and Klein, S.: Progressing Emergent Constraints on Future Climate Change, *Nature Climate Change*, p. 1,
23 <https://doi.org/10.1038/S41558-019-0436-6>, 2019.

24 Harris, I., Jones, P. D., Osborn, T. J., and Lister, D. H.: Updated High-Resolution Grids of Monthly Climatic Observations – the CRU TS3.10
25 Dataset, *International Journal of Climatology*, 34, 623–642, <https://doi.org/10.1002/joc.3711>, 2014.

26 Keeling, C. D., Chin, J. F. S., and Whorf, T. P.: Increased Activity of Northern Vegetation Inferred from Atmospheric CO₂ Measurements,
27 *Nature*, 382, 146–149, <https://doi.org/10.1038/382146a0>, 1996.

28 Keenan, T. F., Prentice, I. C., Canadell, J. G., Williams, C. A., Wang, H., Raupach, M., and Collatz, G. J.: Recent Pause
29 in the Growth Rate of Atmospheric CO₂ Due to Enhanced Terrestrial Carbon Uptake, *Nature Communications*, 7, 13 428,
30 <https://doi.org/10.1038/ncomms13428>, 2016.

31 Klein, S. A. and Hall, A.: Emergent Constraints for Cloud Feedbacks, *Current Climate Change Reports*, 1, 276–287,
32 <https://doi.org/10.1007/s40641-015-0027-1>, 2015.

33 Knutti, R.: The End of Model Democracy?, *Climatic Change*, 102, 395–404, <https://doi.org/10.1007/s10584-010-9800-2>, 2010.

34 Knutti, R., Sedláček, J., Sanderson, B. M., Lorenz, R., Fischer, E. M., and Eyring, V.: A Climate Model Projection Weighting Scheme
35 Accounting for Performance and Interdependence, *Geophysical Research Letters*, 44, 1909–1918, <https://doi.org/10.1002/2016GL072012>,
36 2017.

37 Kwiatkowski, L., Bopp, L., Aumont, O., Ciais, P., Cox, P. M., Laufkötter, C., Li, Y., and Séférian, R.: Emergent Constraints on Projections of
38 Declining Primary Production in the Tropical Oceans, *Nature Climate Change*, 7, 355–358, <https://doi.org/10.1038/nclimate3265>, 2017.

1 Leakey, A. D. B., Ainsworth, E. A., Bernacchi, C. J., Rogers, A., Long, S. P., and Ort, D. R.: Elevated CO₂ Effects on Plant
2 Carbon, Nitrogen, and Water Relations: Six Important Lessons from FACE, *Journal of Experimental Botany*, 60, 2859–2876,
3 <https://doi.org/10.1093/jxb/erp096>, 2009.

4 Lian, X., Piao, S., Huntingford, C., Li, Y., Zeng, Z., Wang, X., Ciais, P., McVicar, T. R., Peng, S., Ottlé, C., Yang, H., Yang, Y., Zhang, Y.,
5 and Wang, T.: Partitioning Global Land Evapotranspiration Using CMIP5 Models Constrained by Observations, *Nature Climate Change*,
6 8, 640–646, <https://doi.org/10.1038/s41558-018-0207-9>, 2018.

7 Mahowald, N., Lo, F., Zheng, Y., Harrison, L., Funk, C., Lombardozi, D., and Goodale, C.: Projections of Leaf Area Index in Earth System
8 Models, *Earth Syst. Dynam.*, 7, 211–229, <https://doi.org/10.5194/esd-7-211-2016>, 2016.

9 Mao, J., Ribes, A., Yan, B., Shi, X., Thornton, P. E., Séférian, R., Ciais, P., Myneni, R. B., Douville, H., Piao, S., Zhu, Z., Dickinson,
10 R. E., Dai, Y., Ricciuto, D. M., Jin, M., Hoffman, F. M., Wang, B., Huang, M., and Lian, X.: Human-Induced Greening of the Northern
11 Extratropical Land Surface, *Nature Climate Change*, 6, 959–963, <https://doi.org/10.1038/nclimate3056>, 2016.

12 Myneni, R., Keeling, C. D., Tucker, C. J., Asrar, G., and Nemani, R. R.: Increased Plant Growth in the Northern High Latitudes from 1981
13 to 1991, *Nature*, 386, 698–702, <https://doi.org/10.1038/386698a0>, 1997a.

14 Myneni, R., Ramakrishna, R., Nemani, R., and Running, S.: Estimation of Global Leaf Area Index and Absorbed Par Using Radiative
15 Transfer Models, *IEEE Transactions on Geoscience and Remote Sensing*, 35, 1380–1393, <https://doi.org/10.1109/36.649788>, 1997b.

16 Myneni, R. B., Hoffman, S., Knyazikhin, Y., Privette, J. L., Glassy, J., Tian, Y., Wang, Y., Song, X., Zhang, Y., Smith, G. R., Lotsch, A., Friedl,
17 M., Morisette, J. T., Votava, P., Nemani, R. R., and Running, S. W.: Global Products of Vegetation Leaf Area and Fraction Absorbed PAR
18 from Year One of MODIS Data, *Remote Sensing of Environment*, 83, 214–231, [https://doi.org/10.1016/S0034-4257\(02\)00074-3](https://doi.org/10.1016/S0034-4257(02)00074-3), 2002.

19 Nemani, R. R., Keeling, C. D., Hashimoto, H., Jolly, W. M., Piper, S. C., Tucker, C. J., Myneni, R. B., and Running,
20 S. W.: Climate-Driven Increases in Global Terrestrial Net Primary Production from 1982 to 1999, *Science*, 300, 1560–1563,
21 <https://doi.org/10.1126/science.1082750>, 2003.

22 Olson, D. M., Dinerstein, E., Wikramanayake, E. D., Burgess, N. D., Powell, G. V. N., Underwood, E. C., D’amico, J. A., Itoua, I.,
23 Strand, H. E., Morrison, J. C., Loucks, C. J., Allnutt, T. F., Ricketts, T. H., Kura, Y., Lamoreux, J. F., Wettengel, W. W., Hedao, P., and
24 Kassem, K. R.: Terrestrial Ecoregions of the World: A New Map of Life on Earth, *BioScience*, 51, 933–938, [https://doi.org/10.1641/0006-3568\(2001\)051\[0933:TEOTWA\]2.0.CO;2](https://doi.org/10.1641/0006-3568(2001)051[0933:TEOTWA]2.0.CO;2), 2001.

26 Park, T., Ganguly, S., Tømmervik, H., Euskirchen, E. S., Høgda, K.-A., Karlsen, S. R., Brovkin, V., Nemani, R. R., and Myneni, R. B.:
27 Changes in Growing Season Duration and Productivity of Northern Vegetation Inferred from Long-Term Remote Sensing Data, *Environ-
28 mental Research Letters*, 11, 084 001, <https://doi.org/10.1088/1748-9326/11/8/084001>, 2016.

29 Piao, S., Nan, H., Huntingford, C., Ciais, P., Friedlingstein, P., Sitch, S., Peng, S., Ahlström, A., Canadell, J. G., Cong, N., Levis, S., Levy,
30 P. E., Liu, L., Lomas, M. R., Mao, J., Myneni, R. B., Peylin, P., Poulter, B., Shi, X., Yin, G., Viovy, N., Wang, T., Wang, X., Zaehle,
31 S., Zeng, N., Zeng, Z., and Chen, A.: Evidence for a Weakening Relationship between Interannual Temperature Variability and Northern
32 Vegetation Activity, *Nature Communications*, 5, 5018, <https://doi.org/10.1038/ncomms6018>, 2014.

33 Pinzon, J. E. and Tucker, C. J.: A Non-Stationary 1981–2012 AVHRR NDVI3g Time Series, *Remote Sensing*, 6, 6929–6960,
34 <https://doi.org/10.3390/rs6086929>, 2014.

35 Poulter, B., Frank, D., Ciais, P., Myneni, R. B., Andela, N., Bi, J., Broquet, G., Canadell, J. G., Chevallier, F., Liu, Y. Y., Running, S. W.,
36 Sitch, S., and van der Werf, G. R.: Contribution of Semi-Arid Ecosystems to Interannual Variability of the Global Carbon Cycle, *Nature*,
37 509, 600–603, <https://doi.org/10.1038/nature13376>, 2014.

1 Qu, X. and Hall, A.: On the Persistent Spread in Snow-Albedo Feedback, *Climate Dynamics*, 42, 69–81, <https://doi.org/10.1007/s00382->
2 013-1774-0, 2014.

3 Sherwood, S. C., Bony, S., and Dufresne, J.-L.: Spread in Model Climate Sensitivity Traced to Atmospheric Convective Mixing, *Nature*, 505,
4 37–42, <https://doi.org/10.1038/nature12829>, 2014.

5 Stephenson, D. B., Collins, M., Rougier, J. C., and Chandler, R. E.: Statistical Problems in the Probabilistic Prediction of Climate Change,
6 *Environmetrics*, 23, 364–372, <https://doi.org/10.1002/env.2153>, 2012.

7 Taylor, K. E., Stouffer, R. J., and Meehl, G. A.: A Summary of the CMIP5 Experiment Design, *PCDMI Rep.*, p. 33, 2009.

8 Taylor, K. E., Stouffer, R. J., and Meehl, G. A.: An Overview of Cmp5 and the Experiment Design, *Bulletin of the American Meteorological*
9 *Society*, 93, 485–498, <https://doi.org/10.1175/BAMS-D-11-00094.1>, 2012.

10 van Vuuren, D. P., Edmonds, J., Kainuma, M., Riahi, K., Thomson, A., Hibbard, K., Hurtt, G. C., Kram, T., Krey, V., Lamarque, J.-F., Masui,
11 T., Meinshausen, M., Nakicenovic, N., Smith, S. J., and Rose, S. K.: The Representative Concentration Pathways: An Overview, *Climatic*
12 *Change*, 109, 5–31, <https://doi.org/10.1007/s10584-011-0148-z>, 2011.

13 Wang, J., Zeng, N., Liu, Y., and Bao, Q.: To What Extent Can Interannual CO₂ Variability Constrain Carbon Cycle Sensitivity to Climate
14 Change in CMIP5 Earth System Models?, *Geophysical Research Letters*, 41, 3535–3544, <https://doi.org/10.1002/2014GL060004>, 2014.

15 Wenzel, S., Cox, P. M., Eyring, V., and Friedlingstein, P.: Emergent Constraints on Climate-Carbon Cycle Feedbacks in the CMIP5 Earth
16 System Models, *Journal of Geophysical Research: Biogeosciences*, 119, 794–807, <https://doi.org/10.1002/2013JG002591>, 2014.

17 Wenzel, S., Eyring, V., Gerber, E. P., and Karpechko, A. Y.: Constraining Future Summer Austral Jet Stream Positions in the CMIP5 Ensemble
18 by Process-Oriented Multiple Diagnostic Regression, *Journal of Climate*, 29, 673–687, <https://doi.org/10.1175/JCLI-D-15-0412.1>, 2015.

19 Wenzel, S., Cox, P. M., Eyring, V., and Friedlingstein, P.: Projected Land Photosynthesis Constrained by Changes in the Seasonal Cycle of
20 Atmospheric CO₂, *Nature*, 538, 499–501, <https://doi.org/10.1038/nature19772>, 2016.

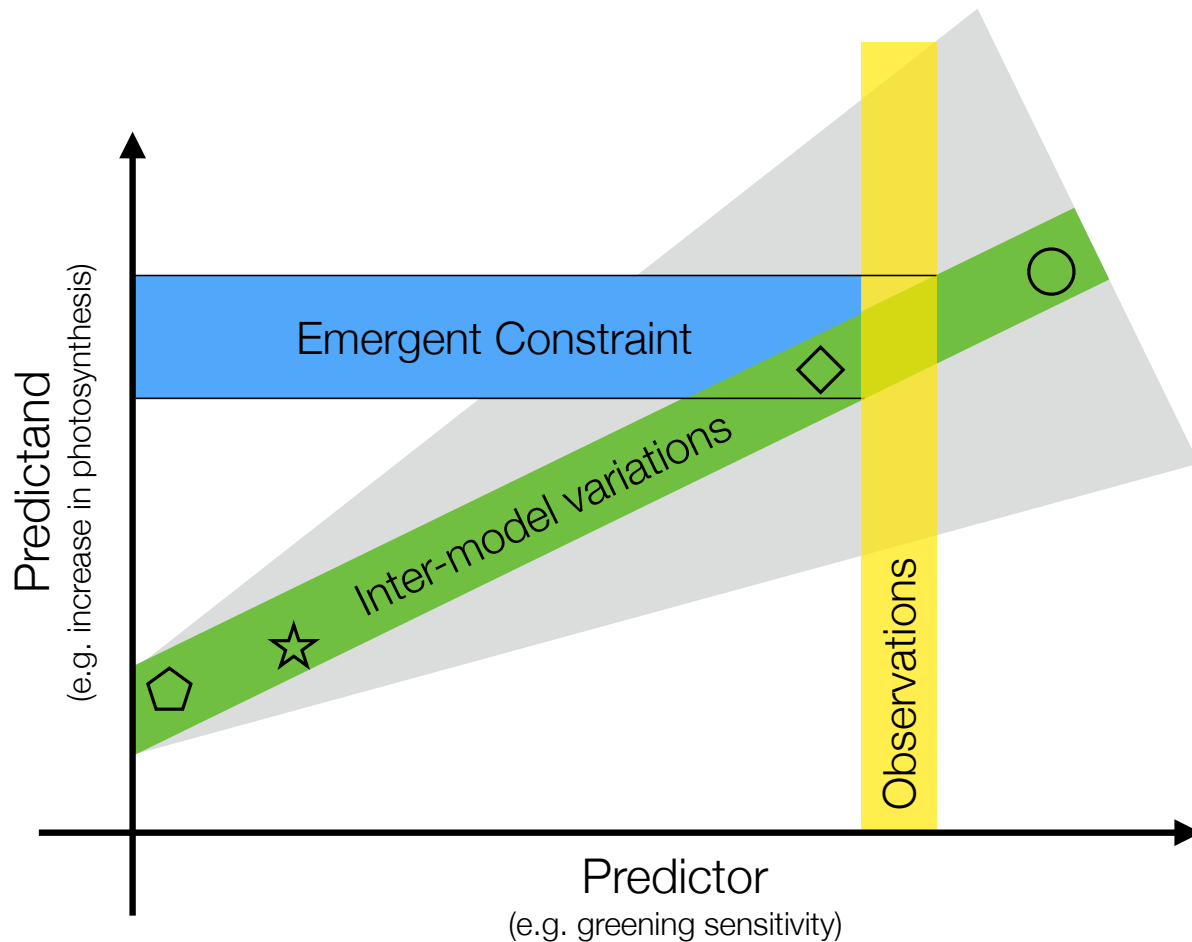
21 Winkler, A. J., Myneni, R. B., Alexandrov, G. A., and Brovkin, V.: Earth System Models Underestimate Carbon Fixation by Plants in the
22 High Latitudes, *Nature Communications*, 10, 885, <https://doi.org/10.1038/S41467-019-08633-Z>, 2019.

23 Yan, K., Park, T., Yan, G., Chen, C., Yang, B., Liu, Z., Nemani, R. R., Knyazikhin, Y., and Myneni, R. B.: Evaluation of MODIS LAI/FPAR
24 Product Collection 6. Part 1: Consistency and Improvements, *Remote Sensing*, 8, 359, <https://doi.org/10.3390/rs8050359>, 2016a.

25 Yan, K., Park, T., Yan, G., Liu, Z., Yang, B., Chen, C., Nemani, R. R., Knyazikhin, Y., and Myneni, R. B.: Evaluation of MODIS LAI/FPAR
26 Product Collection 6. Part 2: Validation and Intercomparison, *Remote Sensing*, 8, 460, <https://doi.org/10.3390/rs8060460>, 2016b.

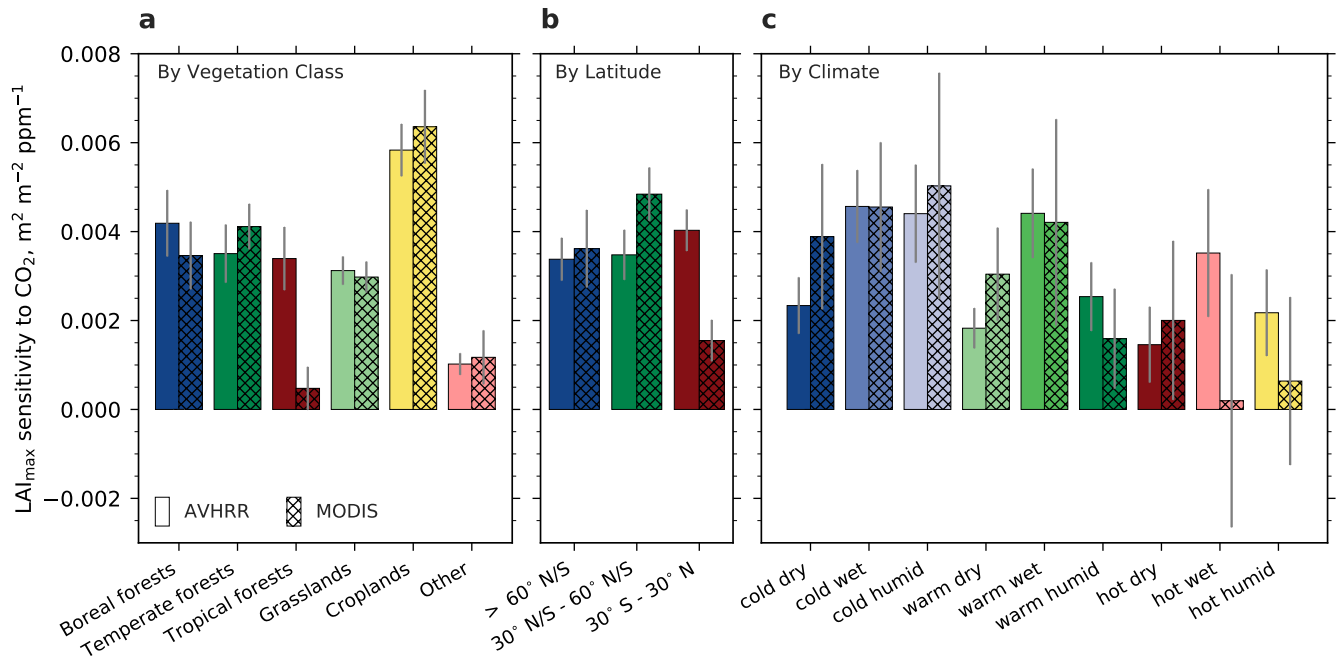
27 Zhu, Z., Bi, J., Pan, Y., Ganguly, S., Anav, A., Xu, L., Samanta, A., Piao, S., Nemani, R. R., and Myneni, R. B.: Global Data Sets of Vegetation
28 Leaf Area Index (LAI)3g and Fraction of Photosynthetically Active Radiation (FPAR)3g Derived from Global Inventory Modeling and
29 Mapping Studies (GIMMS) Normalized Difference Vegetation Index (NDVI3g) for the Period 1981 to 2011, *Remote Sensing*, 5, 927–948,
30 <https://doi.org/10.3390/rs5020927>, 2013.

31 Zhu, Z., Piao, S., Myneni, R. B., Huang, M., Zeng, Z., Canadell, J. G., Ciais, P., Sitch, S., Friedlingstein, P., Arneth, A., Cao, C., Cheng,
32 L., Kato, E., Koven, C., Li, Y., Lian, X., Liu, Y., Liu, R., Mao, J., Pan, Y., Peng, S., Peñuelas, J., Poulter, B., Pugh, T. A. M., Stocker,
33 B. D., Viogy, N., Wang, X., Wang, Y., Xiao, Z., Yang, H., Zaehle, S., and Zeng, N.: Greening of the Earth and Its Drivers, *Nature Climate*
34 *Change*, 6, 791–795, <https://doi.org/10.1038/nclimate3004>, 2016.



1

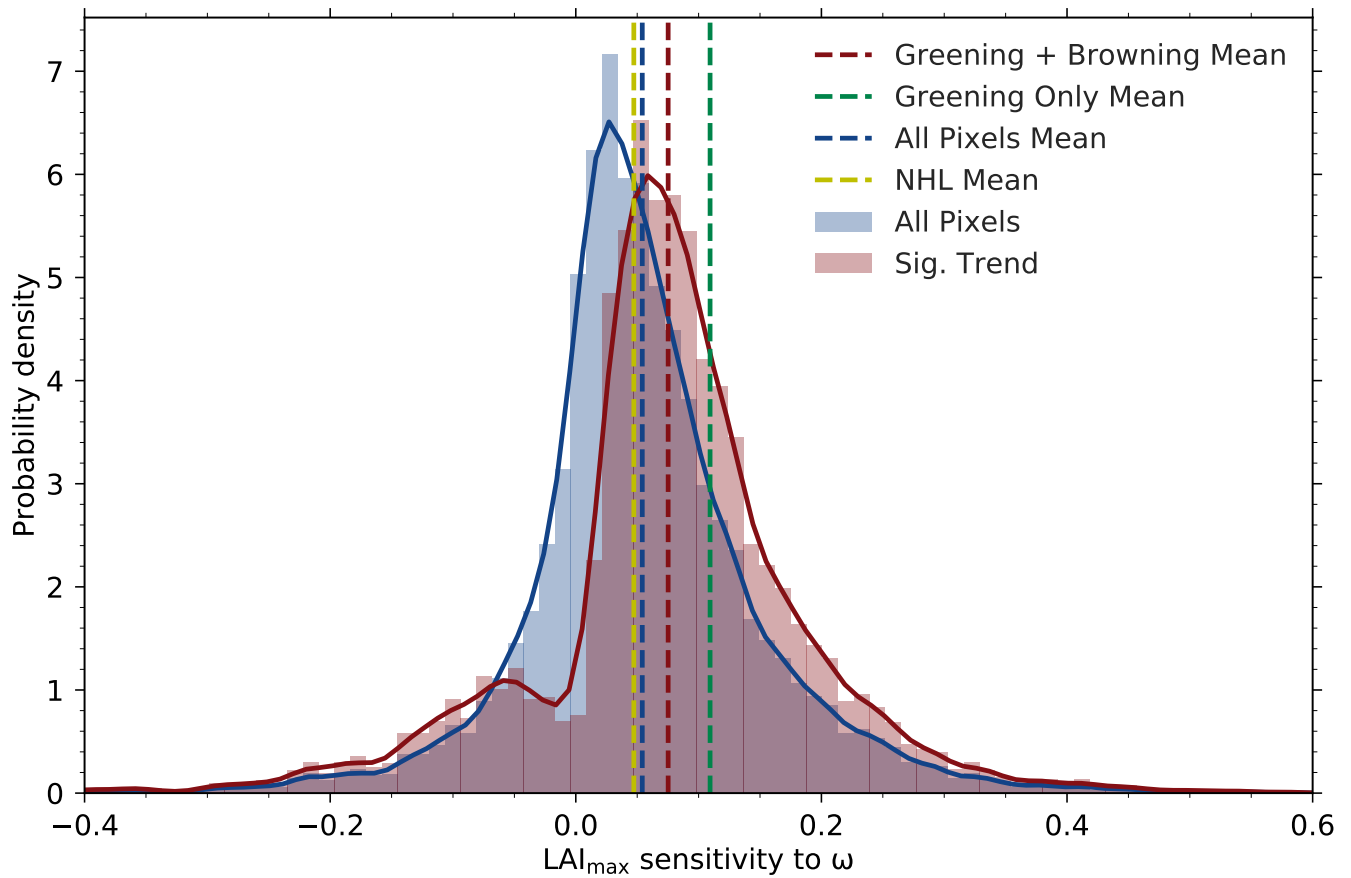
2 **Figure 1.** Schematic depiction of the Emergent Constraint (EC) method and factors affecting the uncertainty of the constrained estimate.
3 The predictor (x axis) is change in annual maximum of green leaf area index (LAI_{max}) due to unit forcing (CO_2 increase and associated
4 climatic changes) during a representative historical period. It is termed greening sensitivity in this study. The predictand (y axis) is projected
5 changes in Gross Primary Productivity (GPP) in response to rising CO_2 concentration (e.g. for a doubling of the pre-industrial level). Both
6 the predictor and predictand refer to large area values, in this case, the entire Northern High Latitudes (NHL). Inter-model variations (each
7 symbol represents a model) in matching pairs of predictor and predictand result in a linear relationship between the two (green band), i.e. the
8 ratio (predictand/predictor) is approximately constant across the model ensemble. The slope depends on forcing attributes (gray shading),
9 such as its level (CO_2 concentration, Sect. 3.4), time rate of application (scenarios such as various RCPs, Sect. 3.4) and different effects (i.e.
10 fertilization, radiative, etc., Sect. 3.5). The observed sensitivity (yellow vertical bar) is used to find the constrained estimate of the predictand
11 (i.e. change in GPP). The ability to accurately estimate the predictor depends on the source of observational data (Sect. 3.1), and its spatial
12 (Sect. 3.2) and temporal variability (Sect. 3.3). Observed (yellow bar) and modeled predictor values (x coordinate of symbols) must be
13 obtained from matching time periods, i.e. at the same level of historical forcing, to ensure comparability (Sect. 3.3 and 3.4). All these factors,
14 together with the goodness-of-fit of inter-model variations (width of green shading), finally define the uncertainty of the derived constrained
15 estimate (blue horizontal bar with black solid lines depicting the upper and lower bound of uncertainty).



1

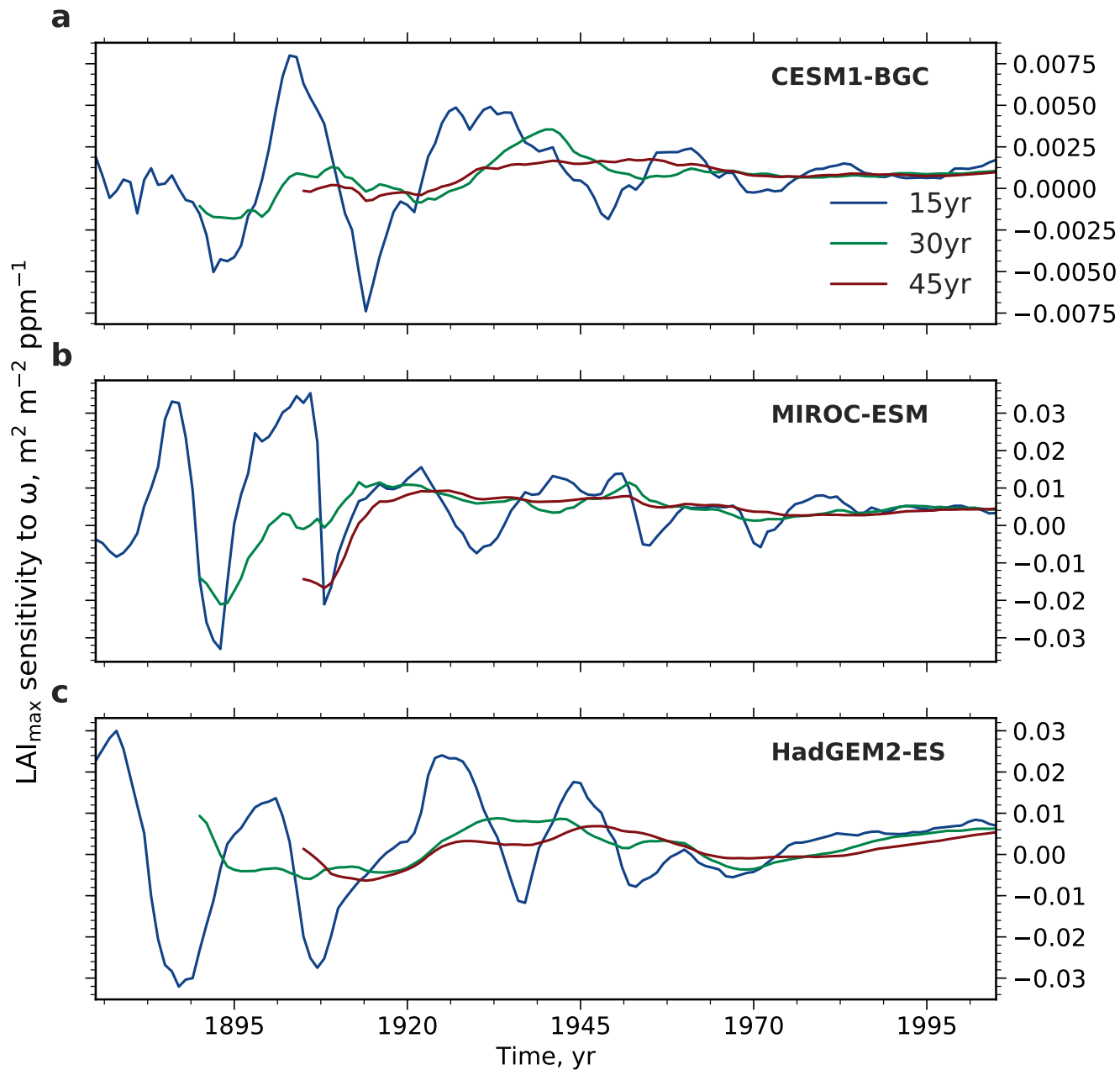
2

3 **Figure 2.** Bar charts showing regression slopes of LAI_{max} against atmospheric CO_2 concentration for broad vegetation classes (**a**; Olson
 4 et al., 2001; Fritz et al., 2015), latitudinal bands (**b**) and climate regimes (**c**). The class "Other" includes deserts, mangroves, barren and urban
 5 land, snow and ice, and permanent wetlands. The climatic boundaries are defined as follows - cold: $< 10^\circ C$; warm: $> 10^\circ C$ & $< 25^\circ C$; hot:
 6 $> 25^\circ C$; dry: $< 500 \text{ mm a}^{-1}$; wet: $> 500 \text{ mm a}^{-1}$ & $< 1000 \text{ mm a}^{-1}$; humid: $> 1000 \text{ mm a}^{-1}$. Sensitivities evaluated from data from two
 7 satellite-borne sensors are shown, AVHRR (1982 – 2016; Pinzon and Tucker, 2014) and MODIS (2000 – 2016; Yan et al., 2016a, b). Grey
 8 bars indicate the standard error of the best linear fit.



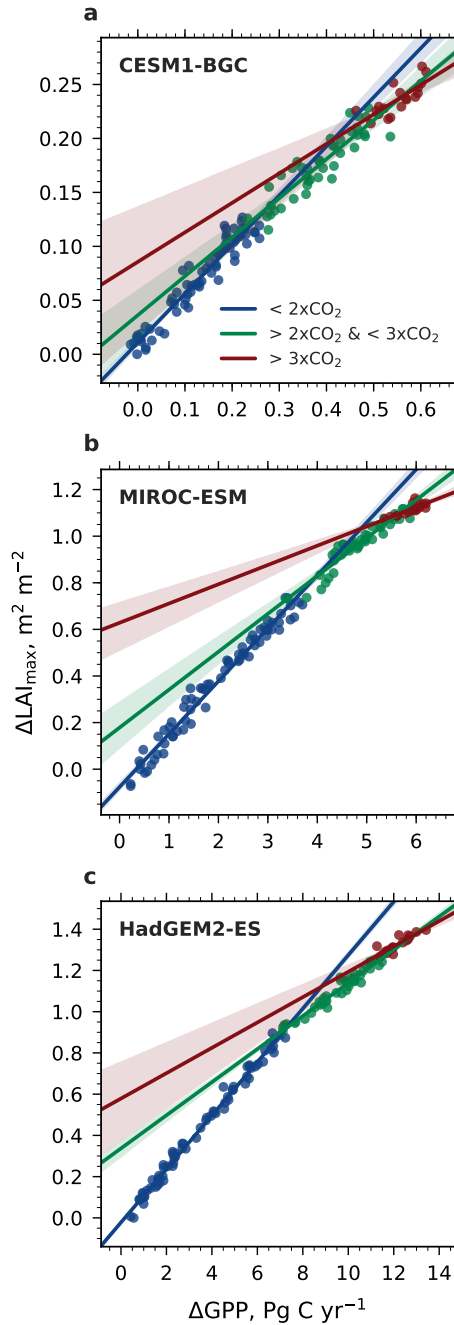
1
2

3 **Figure 3.** Histograms and associated probability density functions (Gaussian kernel density estimation) of observed LAI_{max} sensitivity to
 4 ω at pixel scale for the northern high latitudinal band (> 60° N, data from AVHRR sensor). Blue color depicts the distribution of LAI_{max}
 5 sensitivities of all pixels and the red color for pixels with statistically significant (Mann-Kendall test, $p < 0.1$) greening or browning trends
 6 (the dashed lines denote the respective mean value). The green dashed line shows the mean value of 'greening' pixels only, whereas the
 7 yellow dashed line shows the LAI_{max} sensitivity to ω for the entire northern high latitudinal belt.



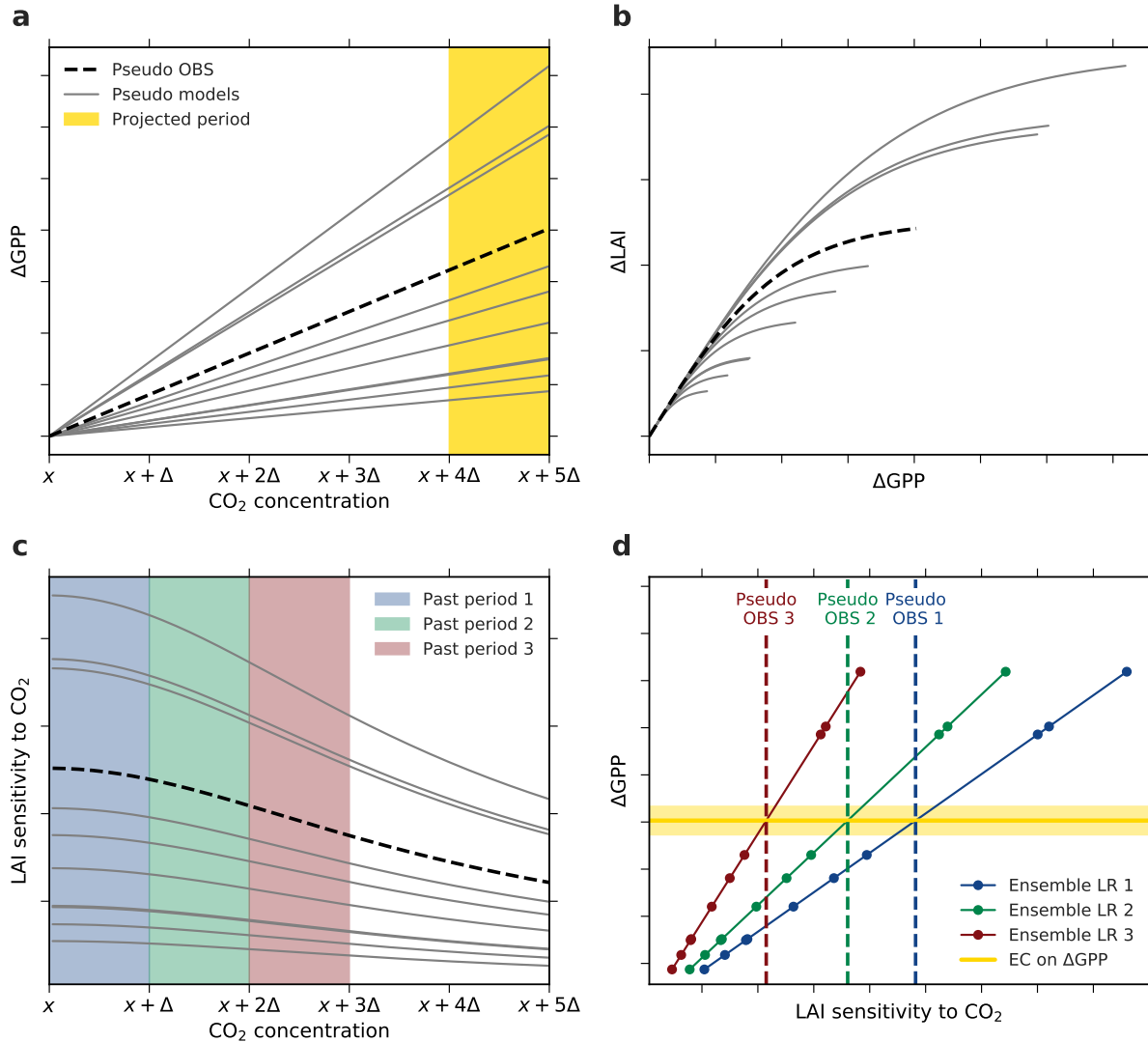
1
2

3 **Figure 4.** Temporal variation of LAI_{\max} sensitivity to ω in three selected CMIP5 models spanning the full range from low (CESM1-BGC,
4 **a**), to closest-to-observations (MIROC-ESM, **b**), to high-end (HadGEM2-ES, **c**). The colored lines show LAI_{\max} sensitivity variations for
5 moving windows of varying length of 15 (blue), 30 (green), and 45 (red) years over the historical period from 1860 to 2005.



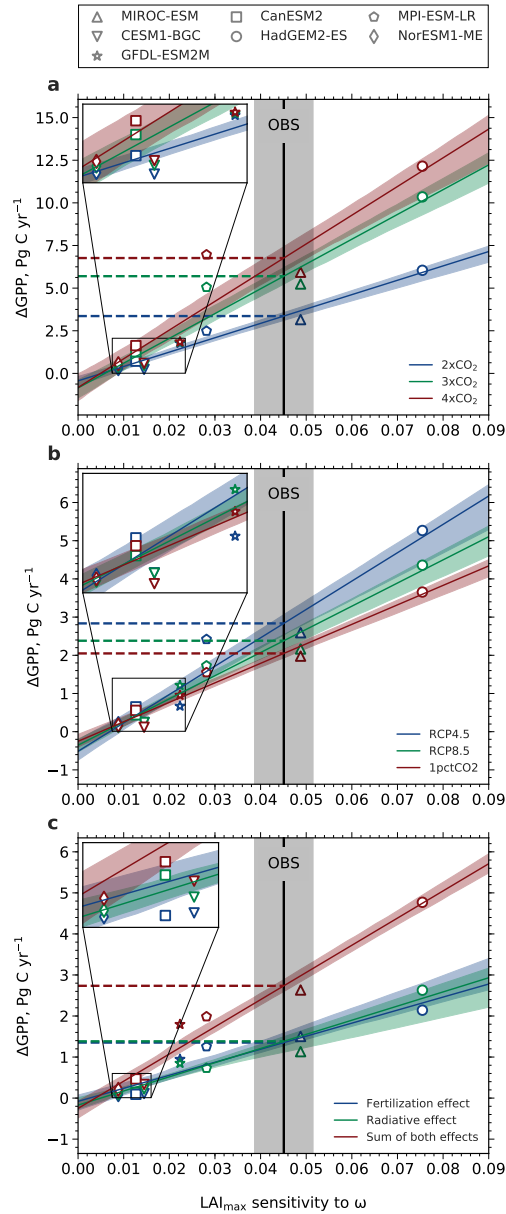
1

2 **Figure 5.** Correlation of $\Delta\text{LAI}_{\text{max}}$ and ΔGPP with increasing CO_2 forcing, starting from a pre-industrial concentration of 280 ppm ($1\times\text{CO}_2$)
 3 to $4\times\text{CO}_2$ (CMIP5 1pctCO2 simulations). Results are shown for three selected CMIP5 models spanning the full range of LAI_{max} sensitivity
 4 to ω , low-end: CESM1-BGC (a), closest-to-observations: MIROC-ESM (b), and high-end: HadGEM2-ES (c). Blue colored dots show the
 5 relation between $1\times\text{CO}_2$ and $2\times\text{CO}_2$, green colored dots between $2\times\text{CO}_2$ and $3\times\text{CO}_2$, and red colored dots between $3\times\text{CO}_2$ and $4\times\text{CO}_2$. The
 6 respective colored lines represent the best linear fit through those dots and the shading represents the 95% confidence interval.



1

2 **Figure 6.** Thought experiment to examine the applicability of EC analysis under the assumption of an idealized linear / non-linear behavior
3 of the system (Case 3, Table A1). **a**, Changes in GPP relate linearly to changes in CO₂ concentration. The yellow band marks the projection
4 period of interest, i.e. the period of CO₂ concentration from $x + 4\Delta$ to $x + 5\Delta$. **b**, The increment in LAI with increasing GPP is assumed
5 to decrease with rising CO₂ concentration (described by a hyperbolic tangent function). The parameterization in the linear and non-linear
6 functions for pseudo observations (dashed black line) as well as models (solid grey lines) are determined randomly for each model. **c**, The
7 diagnostic variable, LAI sensitivity to CO₂, is decreasing with increasing CO₂ as a consequence of the non-linear relation between Δ GPP and
8 Δ LAI. The colored bands indicate three 'past' periods from x to $x + \Delta$ (blue), $x + \Delta$ to $x + 2\Delta$ (green), and $x + 2\Delta$ to $x + 3\Delta$ (red).
9 **d**, Linear relationships among the pseudo model ensembles (Ensemble LR, colored lines) between LAI sensitivities to CO₂ of the three
10 past periods and Δ GPP from the projected period. Colored dots mark different models and the dashed lines represent associated pseudo
11 observations for the respective historical period. Yellow solid line depicts the constant EC on projected Δ GPP irrespective of the past period.



1

2 **Figure 7.** Linear relationships between historical sensitivity of LAI_{max} to ω and absolute increase of GPP at different levels (a), different
3 time-rates (b) as well as effects of rising CO_2 (c). The black solid line depicts the observational sensitivity including the standard error (grey
4 shading). Each CMIP5 model is represented by a distinct marker (legend at the top). The colored lines show the best linear fits including the
5 68% confidence interval estimated by bootstrapping across the model ensemble. The colored dashed lines indicate the derived constraints on
6 ΔGPP . a, Absolute changes in GPP at different levels of CO_2 : $2\times CO_2$ (blue), $3\times CO_2$ (green), and $4\times CO_2$ (red). b, Absolute changes in
7 GPP for rising CO_2 concentration from 380 to 535 ppm at different time-rates: RCP4.5 (90 yr, blue), RCP8.5 (45 yr, green), and 1pctCO2
8 (30 yr, red). c, Absolute changes in GPP due to the two disentangled effects of CO_2 at $2\times CO_2$ in idealized simulations: Fertilization effect
9 (esmFixClim1, blue), radiative effect (esmFdbk1, green), and the sum of both effects (red).

1 **Table 1.** Coefficients of determination (R^2) of LAI_{max} sensitivity to CO₂ for different large-scale aggregated regions. Data are from two
 2 optical remote sensors of different time length, AVHRR (1982 – 2016) and MODIS (2000 – 2016). Asterisks denote non-significant values:
 3 ** p > 0.1; * p > 0.05.

Correlation coefficient R^2	AVHRR	MODIS
Biomes		
Boreal forests	0.49	0.58
Temperate forests	0.47	0.81
Tropical forests	0.41	0.06**
Graslands	0.75	0.83
Croplands	0.75	0.8
Other	0.35	0.2*
Latitudinal Bands		
> 60° N/S	0.51	0.61
30° N/S – 60° N/S	0.67	0.83
30° S – 30° N	0.65	0.26
Climate Space		
cold dry	0.29	0.27
cold wet	0.49	0.4
cold humid	0.33	0.21*
warm dry	0.33	0.36
warm wet	0.37	0.18*
warm humid	0.25	0.12**
hot dry	0.08*	0.08**
hot wet	0.15	0.00**
hot humid	0.13	0.01**

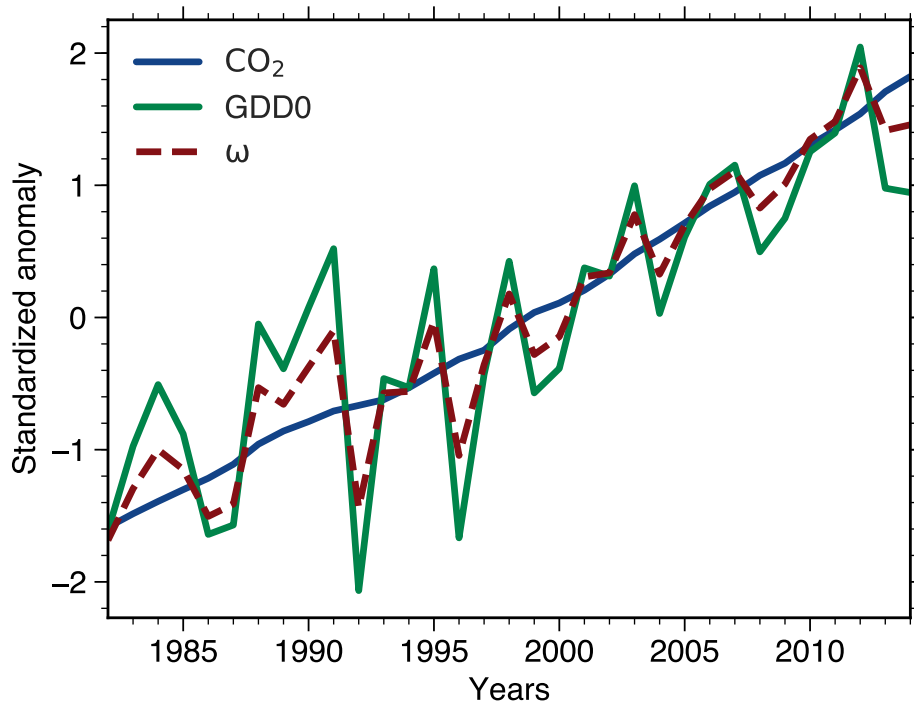
4

1 **Table 2.** Slopes (b) and coefficients of determination (R^2) for regression between changes of LAI_{max} against changes in annual mean GPP
2 for the NHL at different atmospheric CO_2 levels in all available CMIP5 models (1pctCO2 simulation). Asterisks denote non-significant
3 values: ** $p > 0.1$; * $p > 0.05$.

	Correlation details	< 2xCO ₂		> 2xCO ₂ & < 3xCO ₂		> 3xCO ₂	
		b	R^2	b	R^2	b	R^2
	MIROC-ESM	0.23	0.97	0.16	0.89	0.08	0.63
	CESM1-BGC	0.45	0.93	0.36	0.82	0.27	0.62
4	GFDL-ESM2M	0.37	0.89	0.04	0.07**	0.01	0.12**
	CanESM2	0.22	0.95	0.19	0.83	0.17	0.67
	HadGEM2-ES	0.13	0.99	0.08	0.96	0.06	0.78
	MPI-ESM-LR	0.13	0.94	0.09	0.78	0.04	0.51
	NorESM1-ME	0.26	0.94	0.2	0.77	0.09	0.27

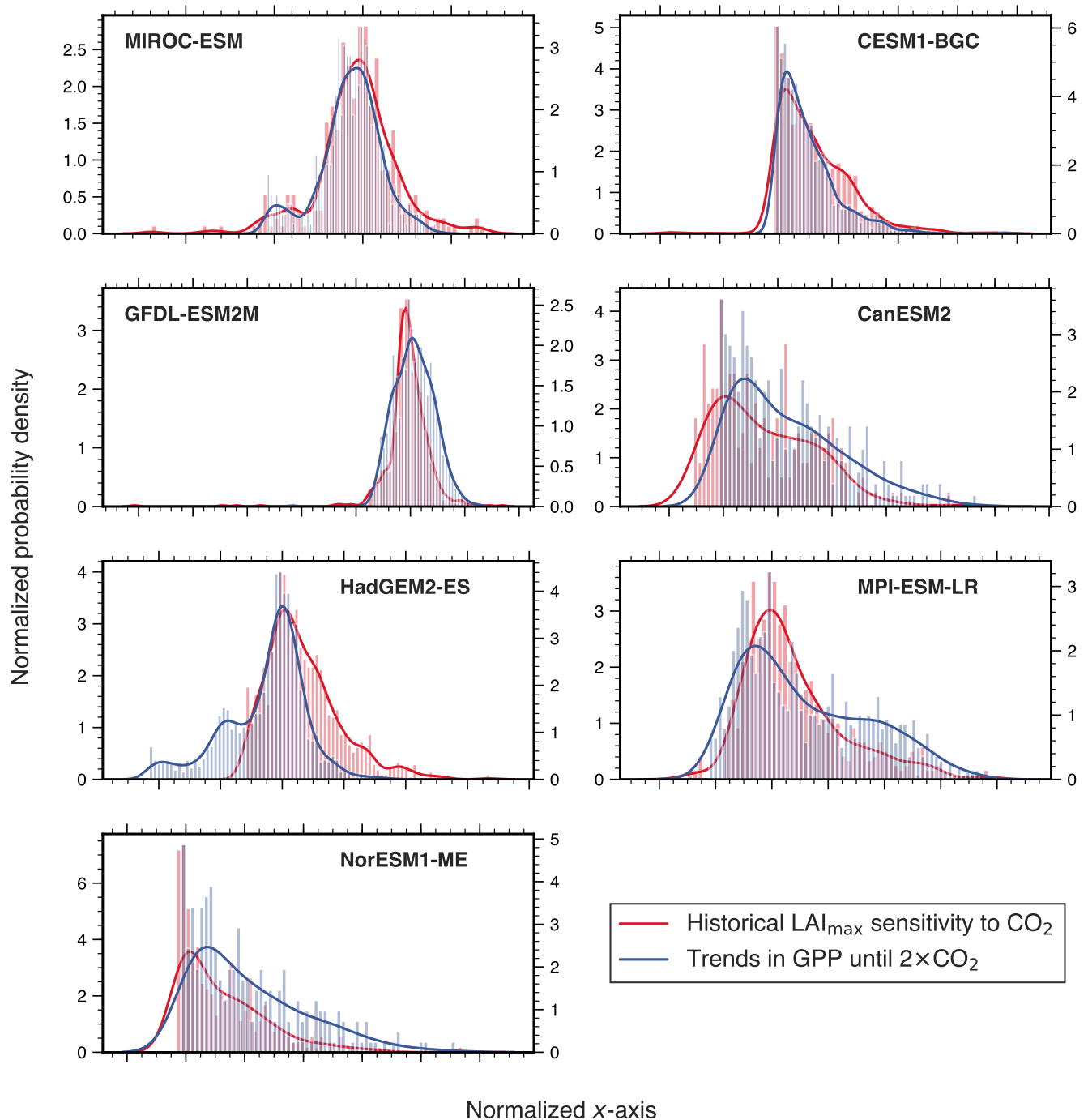
1 **Table 3.** Coefficients of determination (R^2) of the emergent linear relationships in Figure 7 (asterisks denote non-significant values: ** p
2 > 0.1; * p > 0.05). ECs on Δ GPP (upper and lower bound of uncertainty in square brackets) for different atmospheric CO₂ levels and
3 fully-coupled as well as idealized setups. The rightmost column shows the increase of Δ GPP for an increment of $1 \times \text{CO}_2$. The lowermost
4 section compares EC estimates of Δ GPP for equivalent changes in CO₂ concentration (CO₂ rises from 380 to 535 ppm), but for different
5 time-rates.

	R^2	EC Δ GPP estimate (Pg C yr ⁻¹)	EC Δ GPP for $\Delta 1 \times \text{CO}_2$ (Pg C yr ⁻¹)
2xCO₂			
Fully coupled (1pctCO2)	0.96	3.36 [3.15, 3.56]	–
CO ₂ fertilization only (esmFixClim1)	0.88	1.35 [1.29, 1.62]	–
Radiative effect only (esmFdbk1)	0.94	1.38 [1.13, 1.51]	–
Sum of both effects (esmFixClim1 + esmFdbk1)	0.95	2.74 [2.6, 2.9]	–
3xCO₂			
Fully coupled (1pctCO2)	0.93	5.7 [5.26, 6.16]	2.34
CO ₂ fertilization only (esmFixClim1)	0.92	2.15 [2.02, 2.37]	0.79
Radiative effect only (esmFdbk1)	0.98	2.53 [2.3, 2.66]	1.15
6 Sum of both effects (esmFixClim1 + esmFdbk1)	0.96	4.68 [4.38, 4.97]	1.94
4xCO₂			
Fully coupled (1pctCO2)	0.88	6.76 [6.08, 7.53]	1.06
CO ₂ fertilization only (esmFixClim1)	0.88	2.42 [2.23, 2.74]	0.28
Radiative effect only (esmFdbk1)	0.97	3.06 [2.83, 3.2]	0.53
Sum of both effects (esmFixClim1 + esmFdbk1)	0.95	5.49 [5.09, 5.85]	0.81
380 – 535 ppm CO₂			
Slow increase in CO ₂ (RCP4.5)	0.93	2.84 [2.54, 3.08]	–
Medium-fast increase in CO ₂ (RCP8.5)	0.96	2.38 [2.18, 2.55]	–
Rapid increase in CO ₂ (1pctCO2)	0.96	2.05 [1.94, 2.16]	–



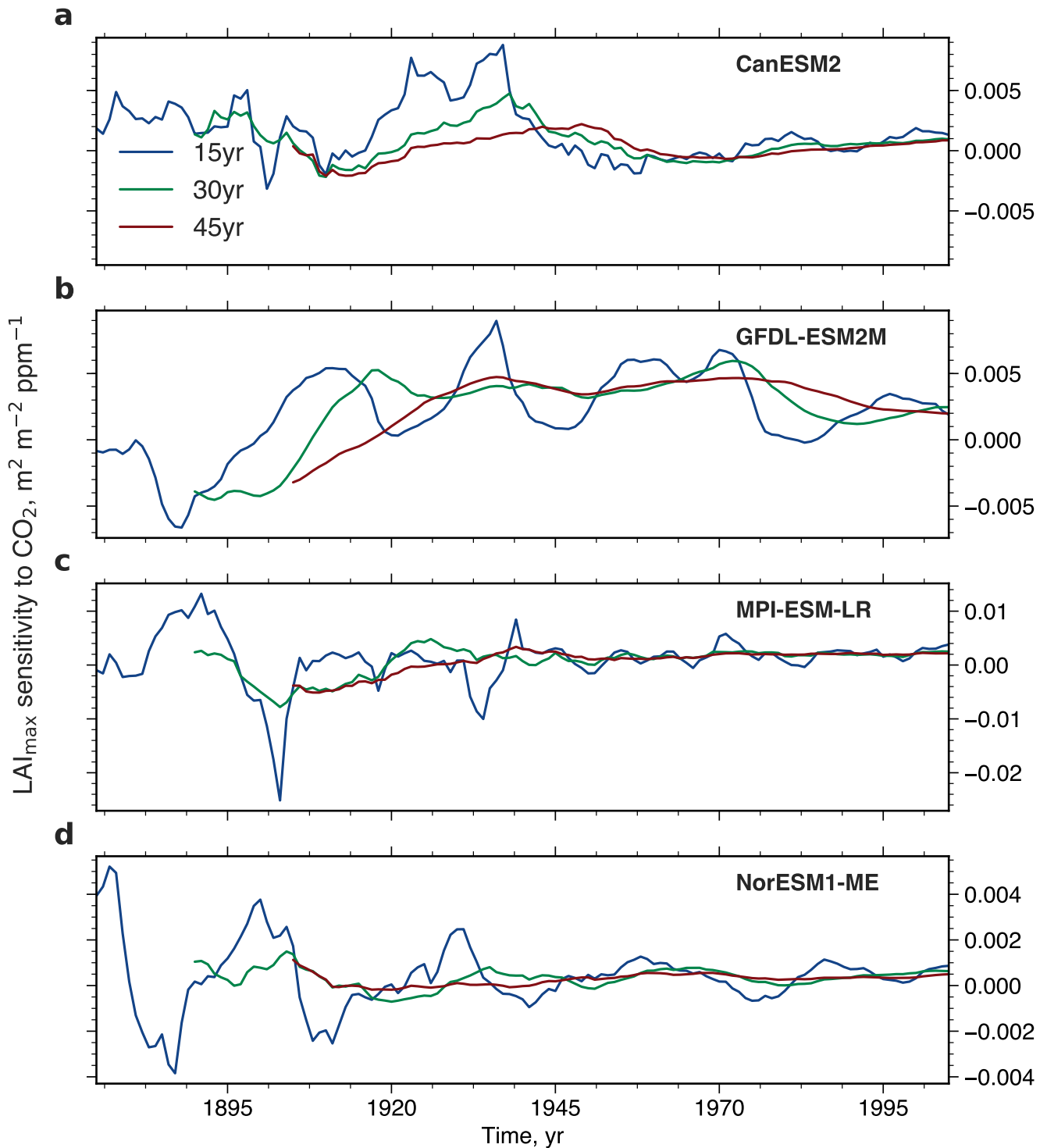
1

2 **Figure A1.** Standardized temporal anomalies of annual averaged atmospheric CO₂ concentration (blue solid line), area-weighted averaged
 3 GDD0 for NHL (green solid line), and their leading principal component ω (red dashed line) in observations.



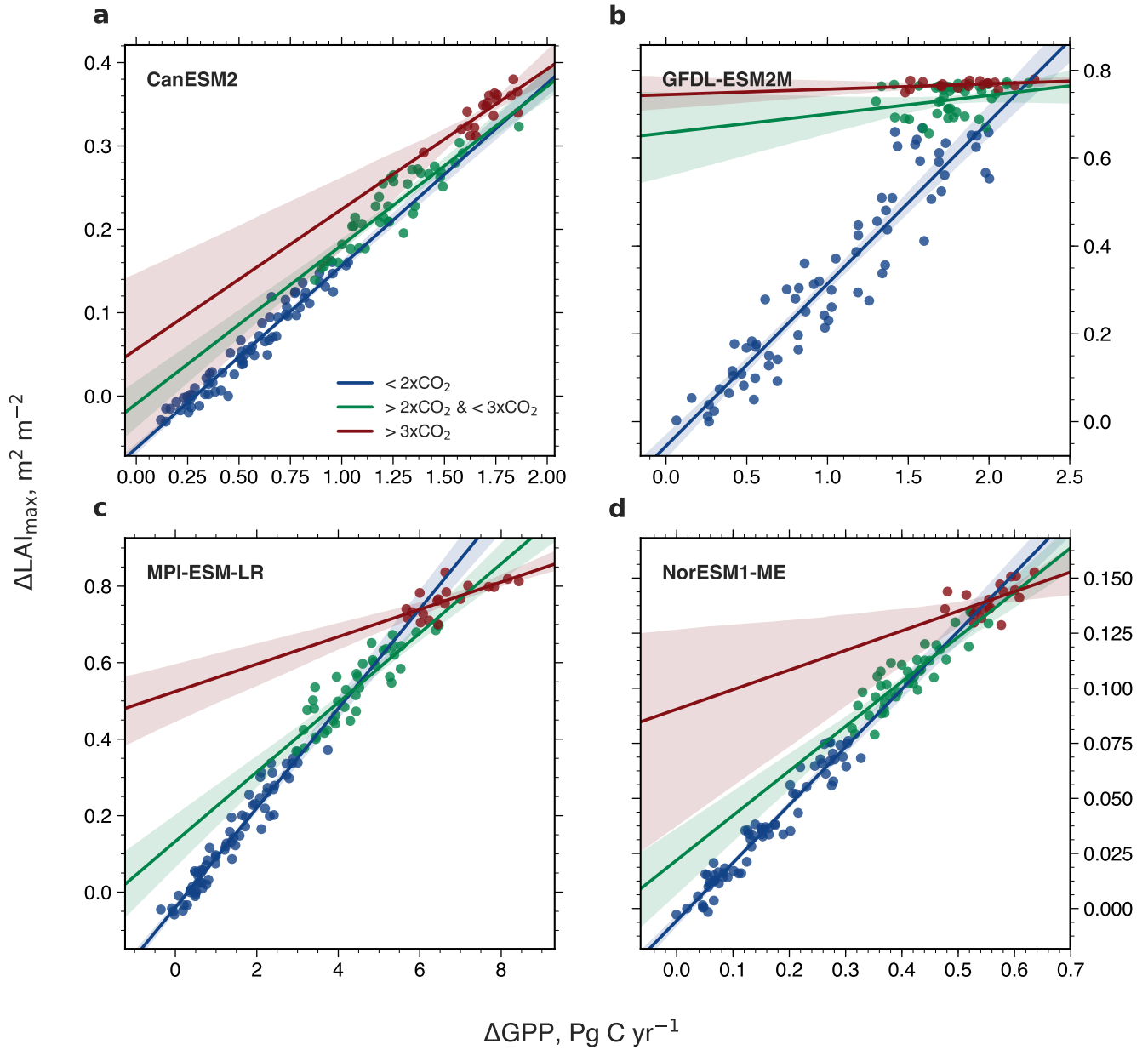
1
2

3 **Figure A2.** Similar pixel distribution of predictor and predictand in each model, except HadGEM2-ES. Histograms and associated probability
 4 density functions (Gaussian kernel density estimation) of LAI sensitivity to ω (red, left y-axis, historical simulations) and temporal trends
 5 in GPP (blue, right y-axis, 1pctCO₂, until 2×CO₂) for NHL are shown for all CMIP5 models. Only significant pixels are included (Mann-
 6 Kendall test, $p < 0.1$). To obtain comparability between the distributions, the x-axis was normalized and has only qualitative meaning.



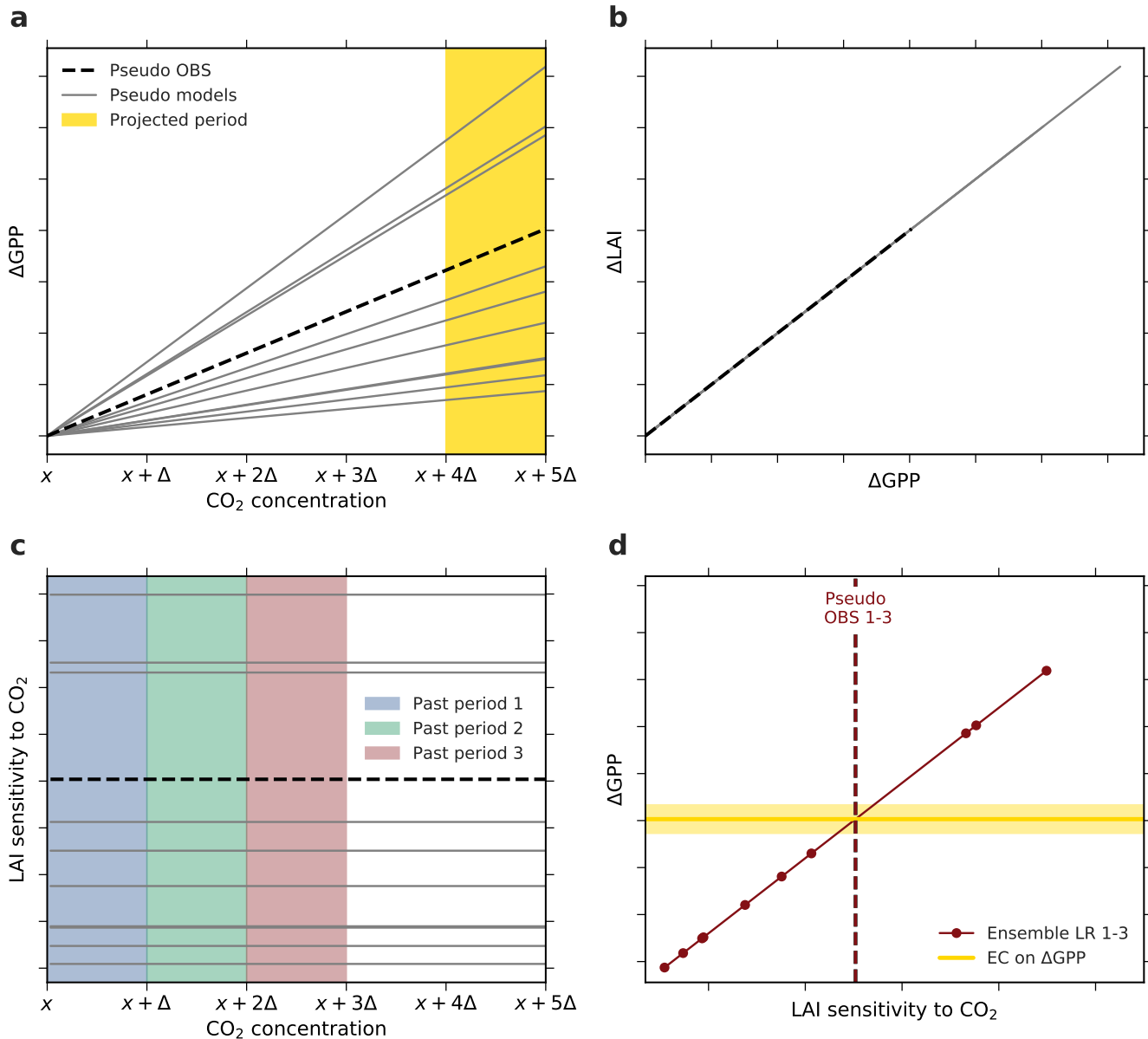
1
2

3 **Figure A3.** Temporal variation of LAI_{max} sensitivity to ω in four CMIP5 models analogous to Fig. 4. The colored lines show LAI_{max}
 4 sensitivity variations for moving windows of varying length of 15 (blue), 30 (green), and 45 (red) years over the historical period from 1860
 5 to 2005.



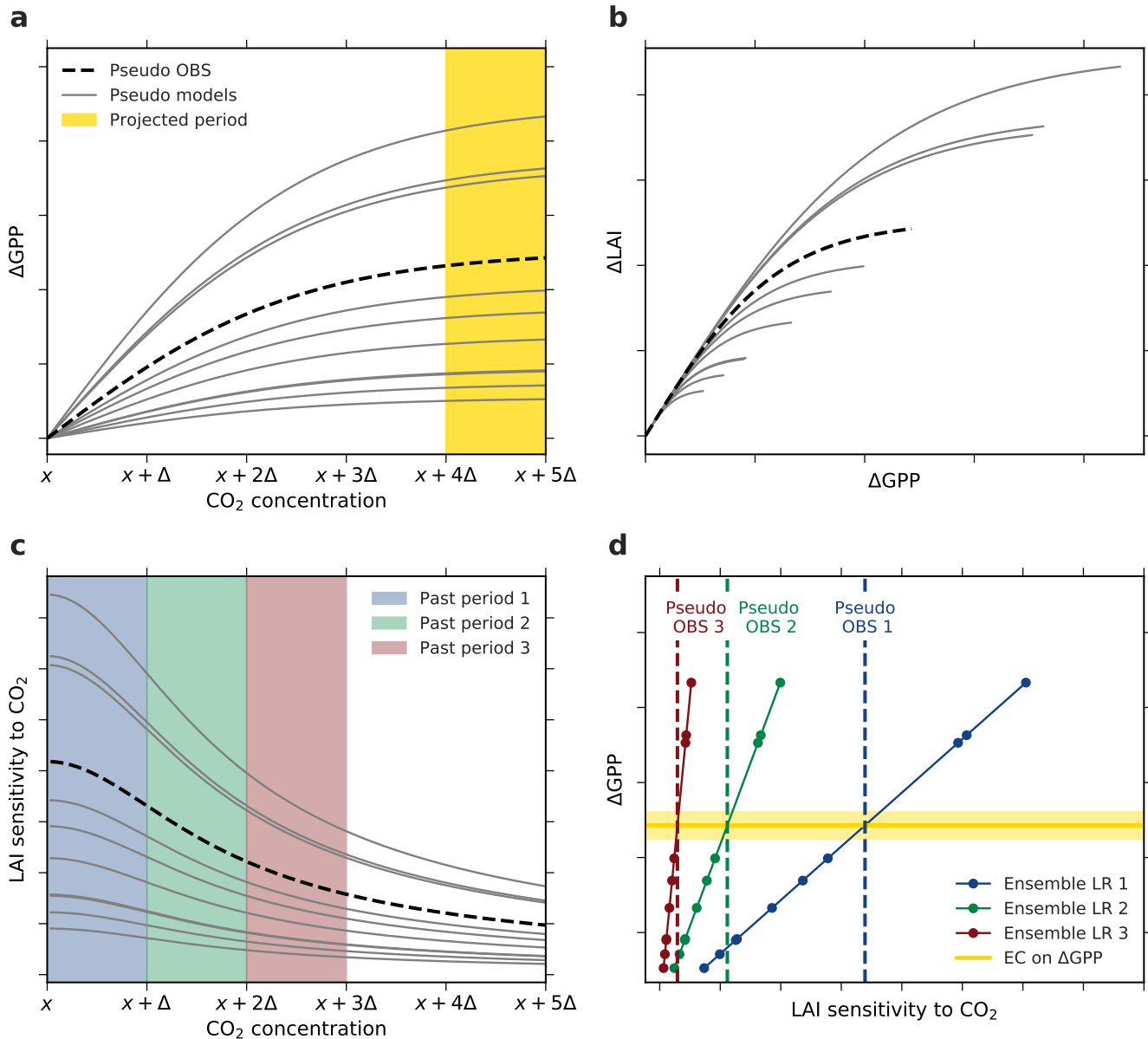
1
2

3 **Figure A4.** Correlation of $\Delta\text{LAI}_{\text{max}}$ and ΔGPP with increasing CO_2 forcing, starting from a pre-industrial concentration of 280 ppm
 4 ($1\times\text{CO}_2$) to $4\times\text{CO}_2$ (CMIP5 1pctCO2 simulations). Results are shown for four CMIP5 models analogous to Fig. 5. Blue colored dots show
 5 the relation between $1\times\text{CO}_2$ and $2\times\text{CO}_2$, green colored dots between $2\times\text{CO}_2$ and $3\times\text{CO}_2$, and red colored dots between $3\times\text{CO}_2$ and $4\times\text{CO}_2$.
 6 The respective colored lines represent the best linear fit through those dots and the shading represents the 95% confidence interval.



1
2

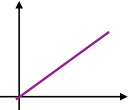
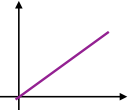
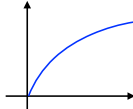
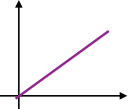
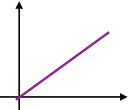
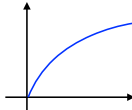
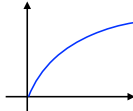
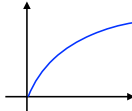
3 **Figure A5.** Thought experiment to examine the applicability of the EC analysis assuming an idealized linear / linear behavior of the system
 4 (Case 1, Table A1). **a**, Changes in GPP relate linearly to changes in CO_2 concentration. The yellow band marks the projection period
 5 of interest, i.e. the period of CO_2 concentration from $x + 4\Delta$ to $x + 5\Delta$. **b**, Changes in LAI relate linearly to changes in GPP. The
 6 parameterization in the linear functions for pseudo observations (dashed black line) as well as models (solid grey lines) are determined
 7 randomly for each model. **c**, The diagnostic variable, LAI sensitivity to CO_2 , remains constant with increasing CO_2 as a consequence of the
 8 overall linear characteristics of the system. The colored bands indicate three 'past' periods from x to $x + \Delta$ (blue), $x + \Delta$ to $x + 2\Delta$
 9 (green), and $x + 2\Delta$ to $x + 3\Delta$ (red). **d**, Linear relationships among the pseudo model ensembles (Ensemble LR 1-3 on top of each other,
 10 red) between LAI sensitivity to CO_2 of the three past periods and ΔGPP from the projected period. Red dots mark different models and the
 11 dashed line represents associated pseudo observations for all three historical periods. Yellow solid line depicts the constant EC on projected
 12 ΔGPP irrespective of the past period.



1
2

3 **Figure A6.** Thought experiment to examine the applicability of the EC analysis assuming an idealized non-linear / non-linear behavior of
 4 the system (Case 4, Table A1). **a**, ΔGPP decreases with increasing CO_2 concentration (described by a hyperbolic tangent function). The
 5 yellow band marks the projected period of interest, i.e. the period of CO_2 concentration from $x + 4\Delta$ to $x + 5\Delta$. **b**, Also ΔLAI decreases
 6 with increasing GPP (described by a hyperbolic tangent function). The parameterization in the hyperbolic tangent functions for pseudo
 7 observations (dashed black line) as well as models (solid grey lines) are determined randomly for each model. **c**, The diagnostic variable,
 8 LAI sensitivity to CO_2 , is decreasing with increasing CO_2 as a consequence of the overall saturating characteristics of the system. The
 9 colored bands indicate three 'past' periods from x to $x + \Delta$ (blue), $x + \Delta$ to $x + 2\Delta$ (green), and $x + 2\Delta$ to $x + 3\Delta$ (red). **d**, Linear
 10 relationships among the pseudo model ensembles (Ensemble LR, colored lines) between LAI sensitivity to CO_2 of the three past periods
 11 and ΔGPP from the projected period. Colored dots mark different models and the dashed lines represent associated pseudo observations for
 12 respective historical period. Yellow solid line depicts the constant EC on projected ΔGPP irrespective of the past period.

1 **Table A1.** Overview of four possible cases of interaction between forcing, non-observable and observable identified in the thought experi-
 2 ment: All linear, all non-linear, and two mixed cases.

Different assumptions	$\frac{d[\text{non-observable}]}{d[\text{forcing}]}$, e.g. $\frac{d[\text{GPP}]}{d[\text{CO}_2]}$	$\frac{d[\text{observable}]}{d[\text{non-observable}]}$, e.g. $\frac{d[\text{LAI}]}{d[\text{GPP}]}$
1	linear 	linear 
2	non-linear 	linear 
3	linear 	non-linear 
4	non-linear 	non-linear 

4